2022

# Experimental and Computational Heat Transfer Study of sCO2 Single Jet Impingement

John Richardson
*University of Central Florida*

STARS Citation
Richardson, John, "Experimental and Computational Heat Transfer Study of sCO2 Single Jet Impingement" (2022). *Electronic Theses and Dissertations, 2020-*. 1431.
https://stars.library.ucf.edu/etd2020/1431

# EXPERIMENTAL AND COMPUTATIONAL HEAT TRANSFER STUDY OF SCO2 SINGLE-JET IMPINGEMENT

by

JOHN RICHARDSON
B.S. University of Central Florida, 2020

A thesis submitted in partial fulfillment of the requirements
for the degree of Master of Science
in the Department of Mechanical and Aerospace Engineering
in the College of Engineering and Computer Science
at the University of Central Florida
Orlando, Florida

Fall Term
2022

Major Professor: Jayanta Kapat

# ABSTRACT

The present study experimentally investigates the heat transfer capability of supercritical carbon dioxide ($sCO_2$) single-jet impingement. The evaluated jet Reynolds number range is between 80,000 and 1,000,000, with a non-dimensional jet-to-target surface spacing of 2.8. $CO_2$-impinging jet stagnation conditions were maintained at approximately 20 MPa and a temperature of 673 K for most experiments. The goal is to understand how changes in the aforementioned parameters influence heat transfer between the working fluid and the heated surface. Additionally, due to the elevated Reynolds numbers and difference in thermodynamic properties between air and $CO_2$, air-derived impingement correlations may not be appropriate for $CO_2$ impingement; these correlations will be evaluated against experimental $sCO_2$ impingement data. At the time of this study, no $sCO_2$ impingement data was available relevant to $sCO_2$ power cycles. The target surface is a 1.5-inch diameter copper block centered on the 3mm jet orifice. A mica heating element bolted to the bottom of the copper block provides a uniform heat flux. Thermocouples embedded in the copper block are used to determine the surface temperature. Nusselt numbers obtained from experimental $sCO_2$ data are compared to area-averaged Nusselt numbers from air-derived correlations. The comparisons showed that air correlations drastically underpredict the heat transfer when $sCO_2$ is used as the working fluid. A modified $sCO_2$ correlation using experimental data at discussed conditions is derived based on an existing air correlation.

To my family and friends, thank you for your love and support through this journey.

# ACKNOWLEDGEMENTS

I want to express my gratitude to Dr. Erik Fernandez, Dr. Jayanta Kapat, and Dr. Samik Bhattacharya for providing their expertise in the development of this thesis. Without the direct support of Dr. Fernandez, this work would have taken much longer to complete; I am incredibly appreciative of his help. Additionally, I am grateful for the guidance provided by Dr. Kapat in examining and interpreting the results of this work. I would also like to give my sincere thanks to Dr. Bhattacharya for taking the time to participate in my committee.

# TABLE OF CONTENTS

# LIST OF FIGURES

# LIST OF TABLES

# NOMENCLATURE

| | |
|---|---|
| $A$ | Area, m$^2$ |
| $b$ | Intercept |
| $D$ | Diameter, m |
| $dT$ | Temperature difference, K |
| $h$ | Heat transfer coefficient, W/m2/k |
| $H$ | Impingement distance or height, m |
| $k$ | Thermal conductivity, W/m/k |
| $m$ | Slope |
| $Nu$ | Nusselt number |
| $Pr$ | Prandtl number |
| $q$ | Heat flux, W/m$^2$ |
| $Q$ | Heat flow rate, W |
| $r$ | Radius, m |
| $R$ | Resistance, Ω |
| $Re$ | Reynolds number |
| $u$ | Uncertainty |
| $V$ | Voltage, V |

**Greek**

| | |
|---|---|
| θ | Sensitivity coefficient |
| Σ | Sum |

**Subscripts, Superscripts, and Accents**

| | |
|---|---|
| *avg* | Average |
| *f* | Fluid |
| *i* | Dependent variable |
| *j* | Jet |
| *l* | Loss |
| *n* | Last number |
| *ref* | Reference temperature |
| *s* | Supply |
| *surf* | Surface |
| *wall* | At wall |
| $\alpha$ | Independent variable |

**Abbreviations**

| | |
|---|---|
| *ASME* | American Society of Mechanical Engineers |
| *CFD* | Computation Fluid Dynamics |
| *DAQ* | Data Acquisition System |
| *dT* | Temperature difference or delta |
| *MEMS* | Micro-Electro-Mechanical System |
| *NIST* | National Institute of Standards and Technology |
| *NPT* | National Pipe Thread |
| *ppm* | Parts per million |
| *RTJ* | Ring Type Joint |
| $sCO_2$ | Supercritical carbon dioxide |

| | |
|---|---|
| *VARIAC* | Variable AC Voltage regulator |

# CHAPTER 1: INTRODUCTION

Power cycles can be said to be the heartbeat of modern civilizations. Engines provide power to vehicles for transportation and turbines for generating electricity. The working fluid, whether air, steam, or some other substance, moves through the various components in a careful design system with the goal of effective and efficient power out. In a power plant, the working fluid in the cycle propels the turbine's blades into angular motion. This motion, paired with an electrical generator, provides most of society's energy needs. Due to the ever-increasing energy demand associated with the progress of society, the need to increase the thermal efficiency of these cycles is of the utmost importance [1].

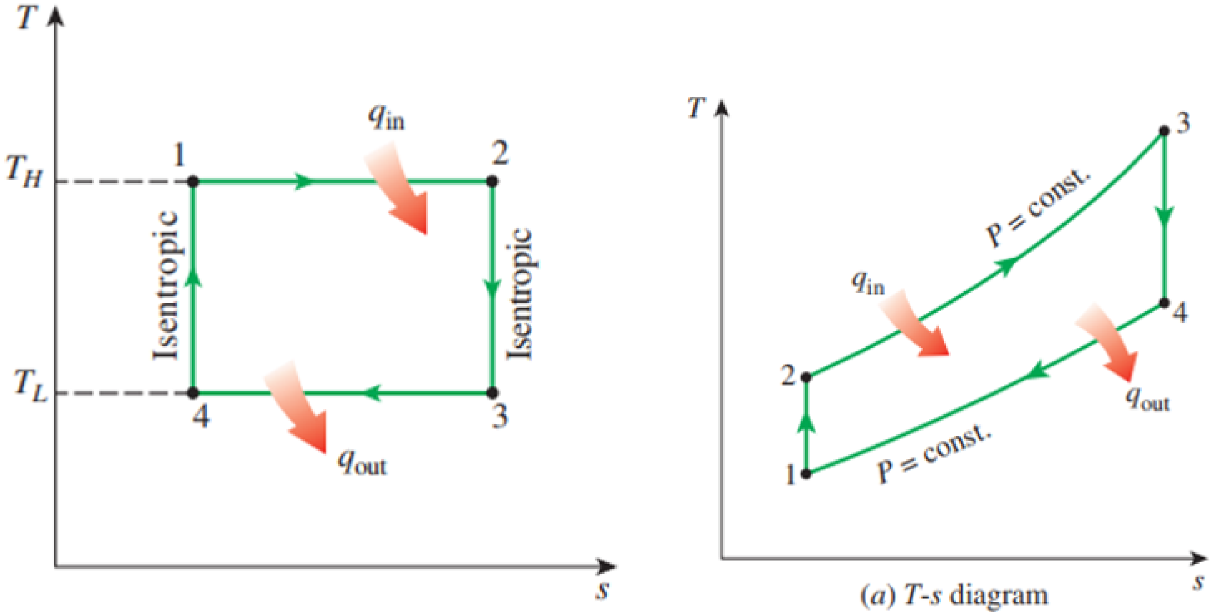

Figure 1.1: T-s diagram for Carnot & Brayton cycles [2]

The Carnot efficiency being a standard, the Brayton cycle can be compared too. The three main avenues for increasing the efficiency of a cycle are: Increasing the turbine inlet temperature, improving the design of turbomachinery components, and augmenting the cycle, e.g., intercooling, regeneration, or reheating. Increasing the inlet temperature into the turbine (i.e., T3 on the Brayton T-s diagram) is the predominant approach to improving efficiency. Several methods are used to improve cooling internal and external for the blade and increase the turbine inlet temperature. The internal methods are impingement, rib turbulators, and pin fins. The internal and external cooling methods are shown in Figure 1.2. Impingement cooling, which is used primarily along the leading edge, is subjected to the highest temperatures; it is also used along the mid-chord of the blade or vane. From there, the cooling flow moves through rib turbulators providing some heat transfer between the cooling fluid and the turbine walls via turbulence. At the trailing edge, pin fin cooling provides heat transfer from the channel end walls to the pins and the cooling fluid. The external method is film cooling; after impingement, the fluid is bled through the film-cooling holes or showerheads, creating a protective coolant layer on the blade.

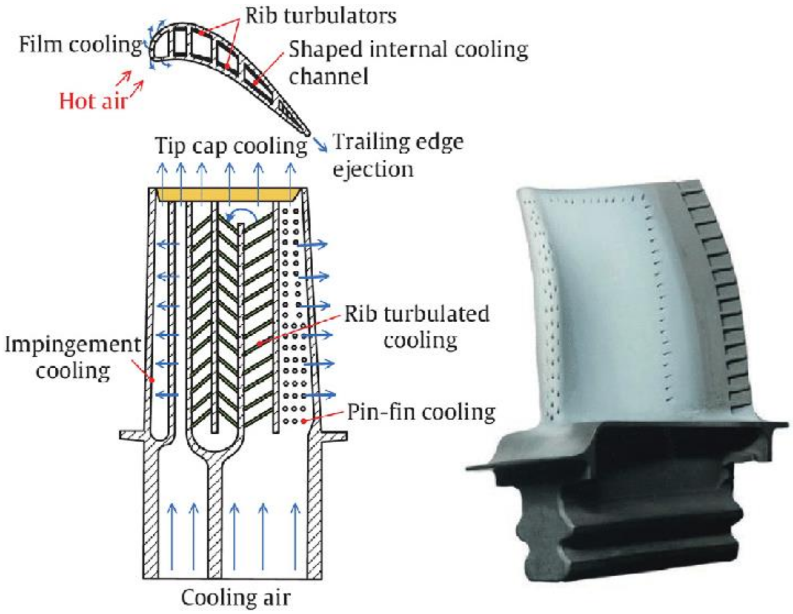

Figure 1.2: Blade cooling methods [3]

The graph below shows the progress of adopted cooling technologies. Beginning with a period in time when blades were taken to their material limits of about 1000K (kelvin) in the 1950s. Then in the 1960s, cooling passages were engineered within the blades providing convection cooling and allowing for the first increases in inlet temperature to around 1300-1400K. Further advances in the 1970s in convection cooling developed internal channels providing more significant heat transfer, enabling inlet temperatures to reach 1500K. Finally, the addition of film cooling in the 1980s pushed temperatures to 1800K, with advances in impingement cooling driving inlet temperatures to 1900K.

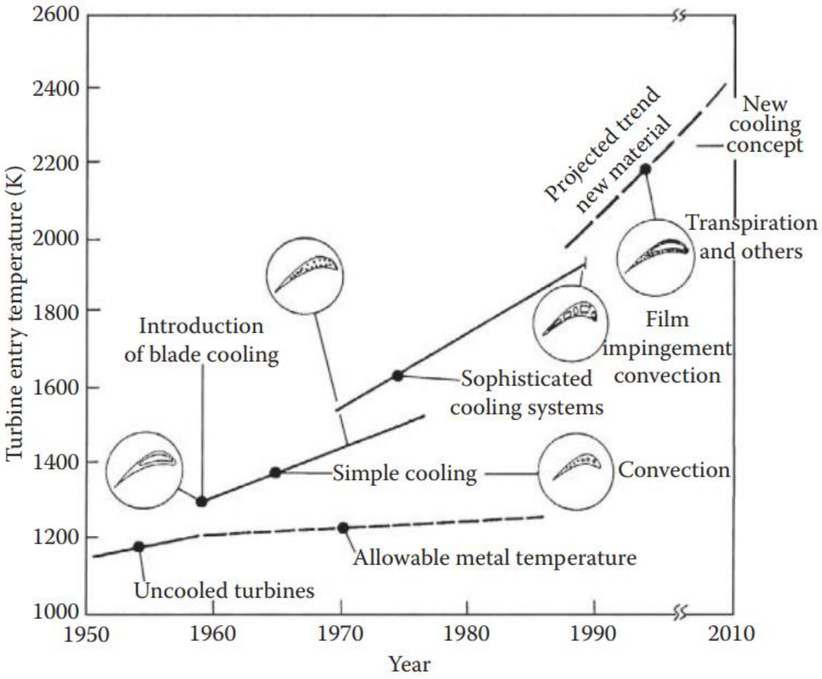

Figure 1.3: Turbine inlet temperature increasing within cooling innovations in cooling performance [4]

An impinging jet is a high-velocity mass ejected from an orifice or slot that impinges on a heat transfer surface. Figure 1.4 shows how an impinging jet would appear on an actual blade. Impingement cooling is used along nearly all paths in contact with the hot inlet gas providing the most significant cooling capability compared to other single-phase heat transfer methods [5]. Therefore, increasing the cooling capacity for jet impingement is of great concern since increasing the inlet temperature in the turbine will provide greater thermal efficiency.

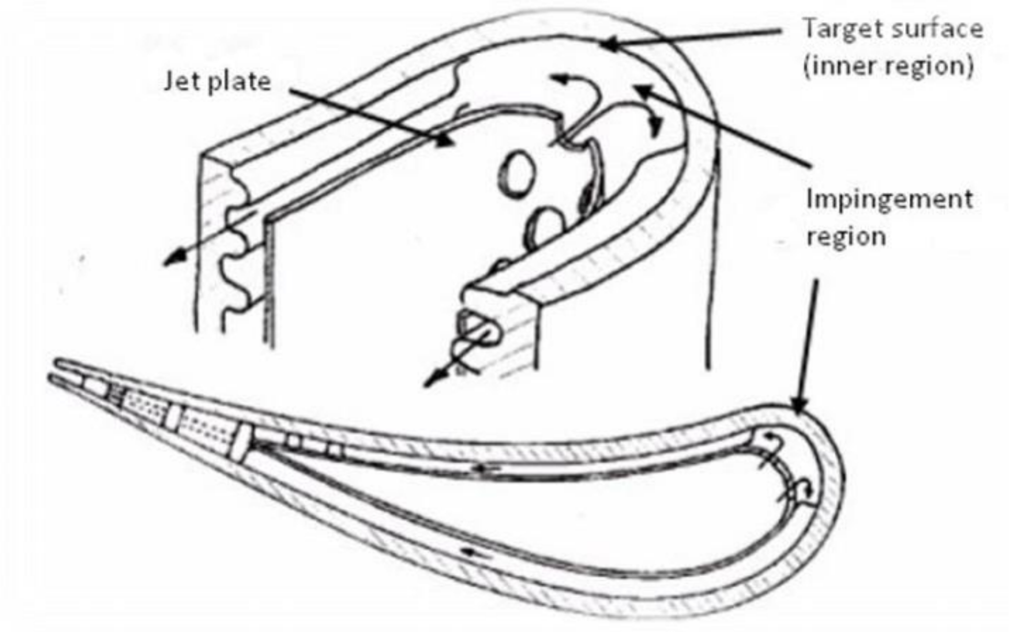

Figure 1.4: Geometry for impinging flow in the blade [6]

## sCO2 in Gas Turbines

In addition to increasing thermal efficiency, lowering cost and pollution outputs are essentials. Indirectly heated $sCO_2$ can replace steam Rankine cycles with higher efficiency and lower plant footprint by exploiting the thermal physical properties of the new working fluid. The working fluid, $CO_{2,}$ at a supercritical state -meaning above its critical pressure and temperature- allows it to expand to fill a volume like a gas and have a density similar to a liquid. As shown in Figure 1.5, this occurs for $CO_2$ above a pressure of 73.8 bar and temperature of 31.1c.

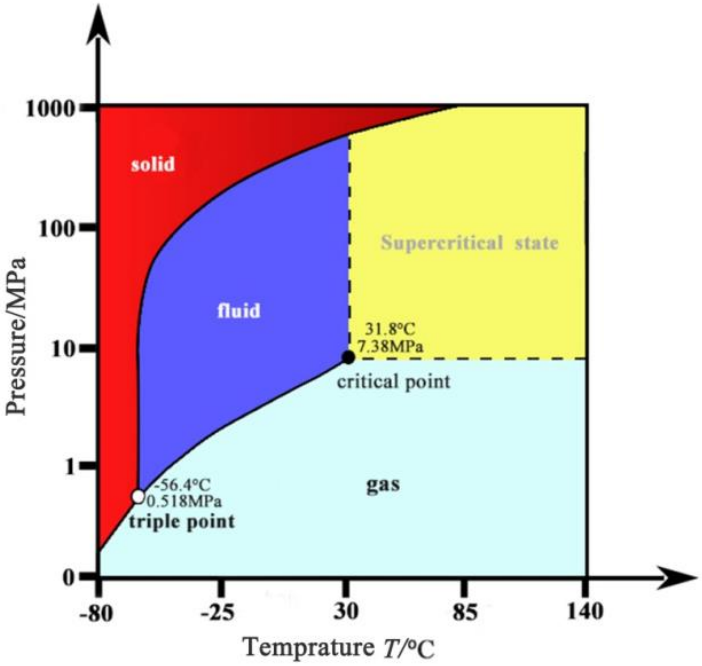

Figure 1.5: Critical point for $CO_2$ [7]

The higher density results in easier compressibility, meaning less compression work and higher cycle efficiency. In addition, small changes in pressure and temperature can significantly impact the density of $sCO_2$. This can be exploited to reduce the size of cycle components, thus reducing plant costs while still producing a significant amount of energy. Interestingly, non-linear changes in $sCO_2$'s thermophysical properties occur along isobars as temperature changes, as shown in Figure 1.6. However, a precise understanding of what drives this theses changes has not been investigated as of this thesis.

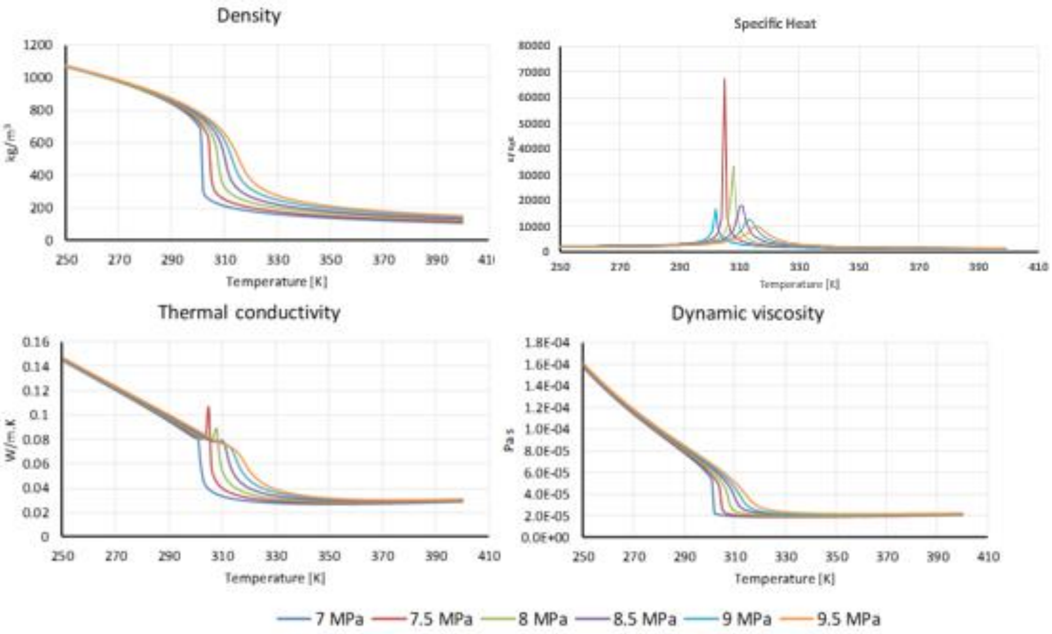

Figure 1.6: Thermophysical properties changing along isobars [8]

# CHAPTER 2: LITERATURE REVIEW

## Flow Field

An impinging jet is a high-velocity mass ejected from an orifice or slot that impinges on a heat transfer surface. Gauntner extensively reviewed the structure of single jet impingement and defined the flow field into three main regions—shown in figure 2.1 below [9].

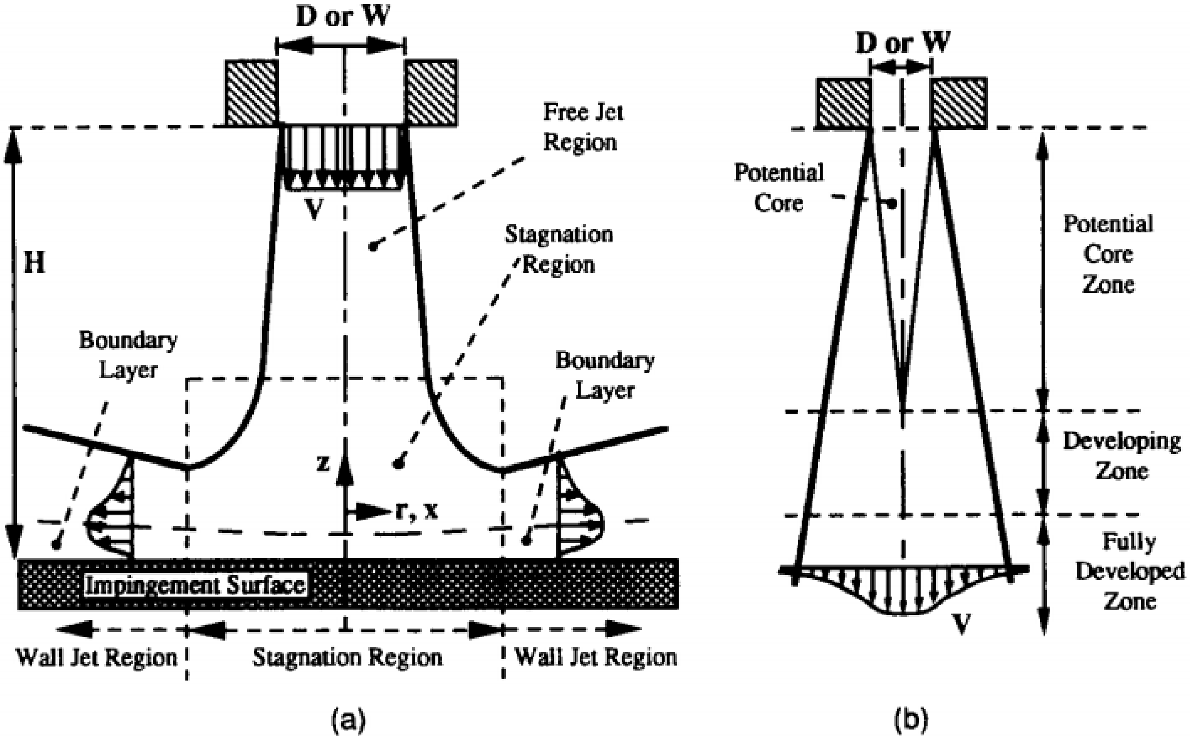

Figure 2.1: (a) Impinging flow field (b) Free jet [10]

The three main regions are the free jet, stagnation, and wall jet regions. The review compared theoretical and experimental works detailing the velocity distribution in the flow regions. In addition, techniques for determining how the jet velocity and pressure profiles develop are provided for impingement cooling designs. The first phase for an impinging flow field is the development of the free jet region. The free jet region occupies the space just before hitting the plate. Axial velocity is highest at the center of a single free jet and decreases radial outward. The decrease is due to shearing and entrainment with the environment, which generates turbulence in the shear layer surrounding the potential core [11]. The potential core, where the nozzle exit velocity is maintained, is an approximate laminar region between the shear layers with a sharp v-like profile. The potential core length is approximately four to eight nozzle widths downstream from the nozzle exit. Viskanta defined the developing and fully developed regions as the final parts of a free jet [10]. The developing region encompasses the decaying jet, and the fully developed region occurs once the decaying jet profile becomes Gaussian. Bradbury covers general velocity distribution and jet axial velocity decay, providing vital information on single-free jet fluid mechanics [12].

Figure 2.1(a) shows after hitting the surface, the structure of the stagnation region forms, and the outward spent jet creates the wall jet regions that further turbulates the fluid in the environment. Flow is highly turbulent at and near the impingement region; the stagnation region typically begins 1.2 diameter lengths above the surface for a round jet [13]. The stagnation region marks the beginning of a nonuniform flow turning, accompanied by large normal and shear stresses that heavily influence the local transport properties: viscosity, thermal conductivity, and diffusivity. In addition, vortex stretching occurs due to the nonuniform flow path within the region's increasing turbulence. Maurel and Solliec's experimental work outlines the influences and development of the Reynolds stresses within the stagnation region[14]. After impingement, a thin boundary layer is formed within the stagnation and wall jet region. The boundary layer thickness is inversely proportional to the square root of the Reynolds number. In practical applications, Reynolds numbers can be on the order of magnitude of $10^4$ or more; the boundary layer thickness can be as low as one-hundredth of the nozzle diameter. The outward flow from the stagnation region eventually develops the wall jet region. The thickness of the region can be determined by measuring the height where the flow speed is 5% of the max speed in the wall jet parallel to the surface. The boundary layer in the stagnation region increases to a maximum of 1% of the jet diameter within the wall jet region [13].

## Heat Transfer

The heat transfer coefficient is defined as follows:

$$h = \frac{Q}{A \times \left(T_{wall} - T_{ref}\right)} \tag{2.1}$$

Where $T_{ref}$ can be either the jet or adiabatic temperature, the heat transfer coefficient is nondimensionalized using the Nusselt Number:

$$Nu = \frac{hD}{k_f} \tag{2.2}$$

Additionally, a power-law relationship is typically used to determine an empirical Nusselt number correlation for characterizing experimental results [15].

### *Air*

The effects turbulences have on heat transfer in the stagnation region for round jets were studied by Kataoka [16]. The work shows heat transfer enhancement by large-scale eddies by renewing turbulence on the surface. Hrycak's literature review discussed the results of Huang, Gardon, and Waltz [17]. Huang observed that an adjustment within $1 < z/D < 10$ showed minimal impact on the heat transfer coefficient, with a general agreement for Daane and Han's work [18]. Conversely, Gardon showed peak heat transfer rate increasing as z/D decreased with

Waltz work supporting. Gardon stated later that the heat flow gauge could have had a calibration error of 40%[17]. Hrycak's literature review also discussed the results of Brdlik and Savin, which showed that for $z/D < 6.2$, there was little to no impact on the heat transfer coefficient when the standoff distance was adjusted within the stated range for laminar flow [19].

Additionally, Kataoka showed that a z/D between 5-8 will produce a maximum stagnation point Nusselt number, and a maximum turbulent intensity occurs at a z/D of 7. Viskanta reviewed the effect of Reynolds number and z/D [10]. For circular jets, various Reynolds numbers and z/D less than one can produce dominating secondary peak in the heat transfer distribution. This is because the acceleration of the fluid from the impingement surface creates a thinning boundary layer at $r/D = 0.5$. The secondary peaks can be attributed to this acceleration, but it may not be the only reason. Additionally, increasing the Reynolds numbers increases the amplitude of the secondary peaks [20].

### *s$CO_2$*

A small number of experimental studies pertaining to s$CO_2$ jet impingement around the pseudocritical point have been conducted. Chen et al. demonstrate that the local heat transfer coefficient increases near the stagnation point when the inlet temperature is lower than the pseudocritical temp and the impinging surface temperature is slightly higher than it [21]. Chen also performed a numerical study validated by the above-mentioned experimental results [22]. Kim numerically studied s$CO_2$ jet impingement in oxy-fuel s$CO_2$ turbines, focusing on changes in the heat transfer coefficient when heat flux varies [23]. They found secondary peaks appear at a radial location further down than air, and the s$CO_2$ inlet values should be determined with respect to the heat flux range of the impinging surface. Potential experimental studies may consider examining extreme cases, such as ultra-high Reynolds numbers. Cormier showed that a

RANS model simulation with a $v^2$-turbulent viscosity model handled ultra-high Reynolds numbers and temperatures the best [24]. Though a number of experimental studies using $sCO_2$ for micro cooling applications have been conducted [21, 25], there is a lack of practical studies for cooling applications for gas turbines. The work presented in this thesis aims to provide experimental heat transfer data for gas turbine applications. The primary conditions of this study are 200 bar with a jet temperature of 400c. Data at these conditions will be valuable to the heat transfer database for jet impingement studies at gas turbine conditions.

# CHAPTER 3: RESEARCH OBJECTIVE

## Intellectual Merit

In recent years, the efficiency and cost of $sCO_2$ power cycles have developed such that they are now capable replacements for ultra-supercritical steam cycles. Further advancement in indirectly heated $sCO_2$ cycles will provide cycles that cleanly convert fossil fuels. With the Supercritical Transformational Electric Power (STEP) pilot plant being commissioned sometime in 2022, commercial $sCO_2$ power plants are fast approaching. Given that such plants can have turbine inlet temperatures around 700c [26], effective cooling of turbine blades is necessary. In order to do so, it is essential to study the heat transfer characteristics of the jet impinging internally on the blade. This experimental investigation varies Reynolds numbers for a single jet to surface spacings (z/D or H/D), providing area average heat transfer data quantifying how well this specific impingement setup cools an isothermal surface. In addition, this study will determine if air-derived correlations can accurately quantify $sCO_2$ heat transfer and provide an adjusted correlation specifically for the conditions of the investigation.

# CHAPTER 4: METHODOLOGY

This chapter begins with the specifics of the benchtop test and the copper block assembly. Followed by the experimental setup and procedures for the air validation tests and the $sCO_2$ tests are discussed. Finally, critical empirical analyses are provided; the sections included are the 'Heat Loss Test,' 'Data Reduction,' and 'Uncertainty Analysis.'

## Benchtop Test

The components for the copper block assembly are shown in Figure 4.1. Figure 4.2 shows the copper block instrumented with the mica heater. The mica heater is held in place by the threading at the bottom of the copper block, as shown in Figure 4.5. The copper block assembly for the experimental test is shown in Figure 4.3. Figure 4.4 is a schematic of the Benchtop experimental setup.

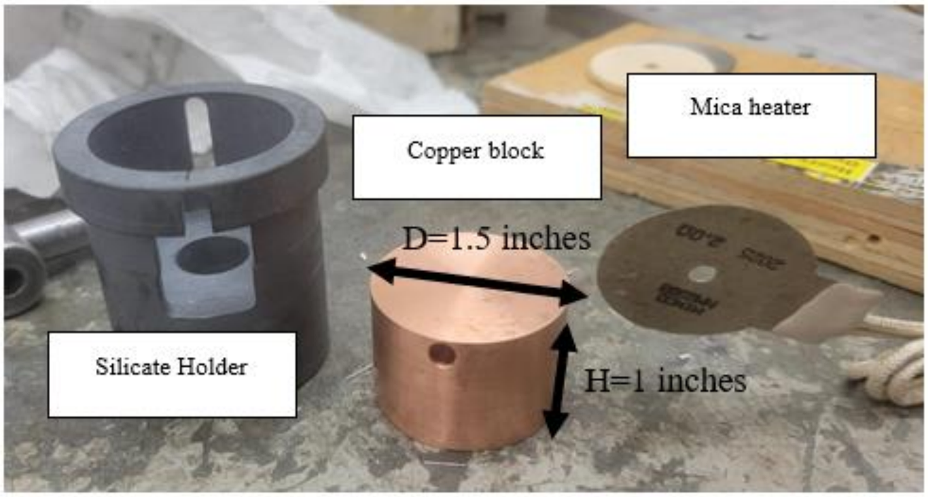

Figure 4.1: Copper block assembly components

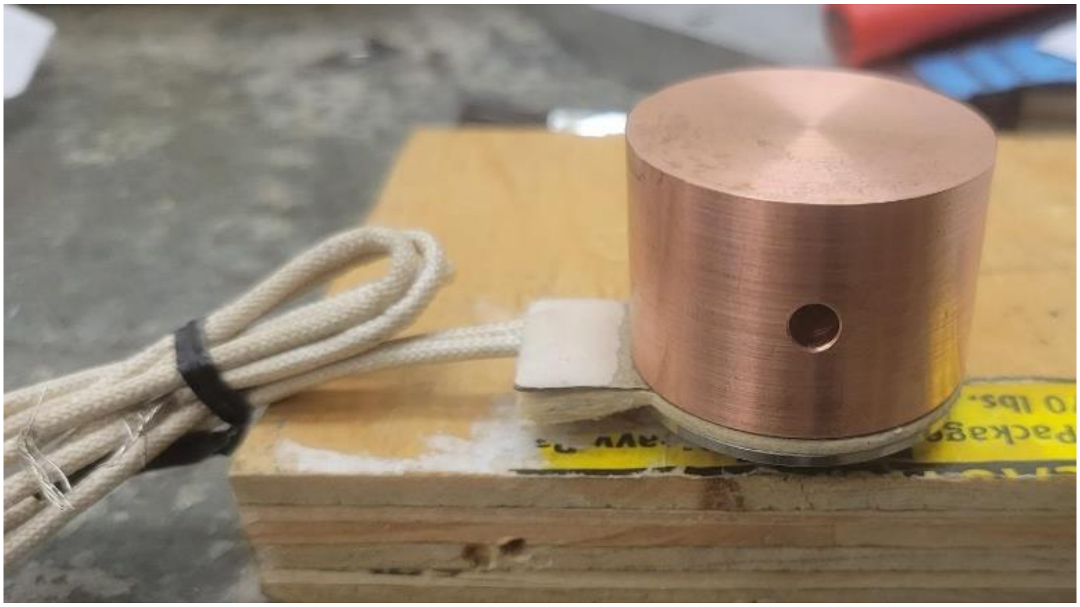

Figure 4.2: Copper block instrumented with mica heater

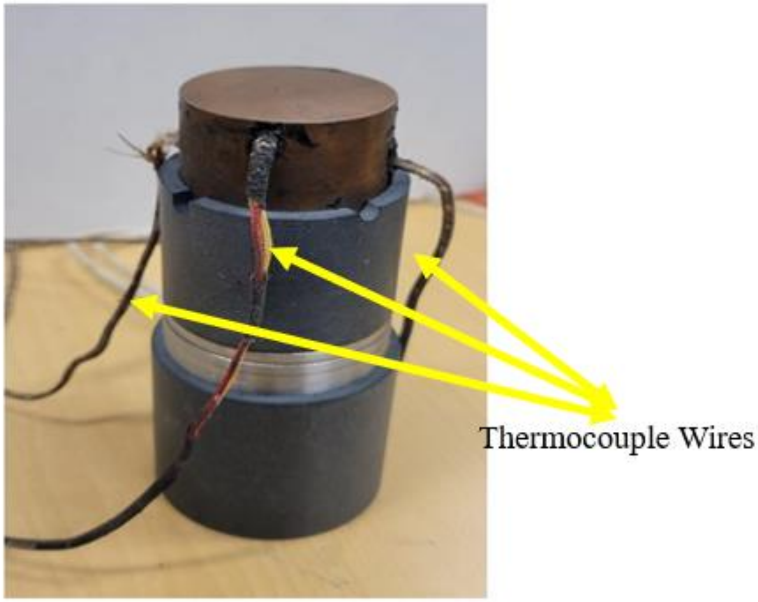

Figure 4.3: Benchtop experimental setup

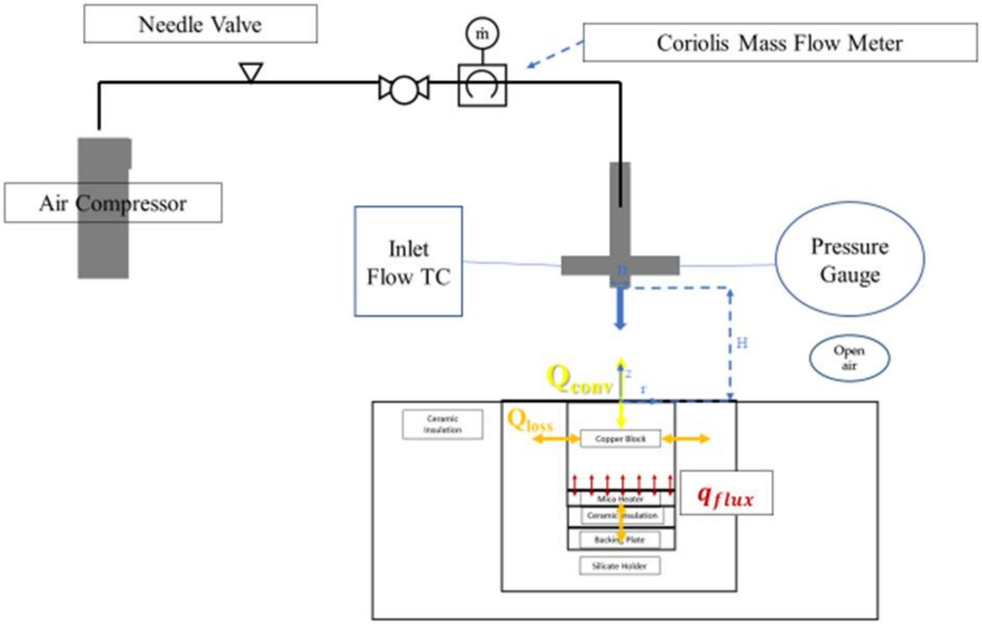

Figure 4.4: Benchtop experimental schematic

To begin the experiment, the compressor is turned on, and the flow rate is adjusted using the needle valve and measured using the mass flow meter. The flow then exits the nozzle travels along the z-axis shown in Figure 4.4, and impinges on the copper block. The copper block is a cylinder with a radius of 0.75in and a height of 1in (inch). Copper was selected due to its high thermal conductivity allowing for isothermal conditions. At the time of this study, other $sCO_2$ experiments were performed at pressure and temperature conditions substantially lower than turbine inlet conditions; thus, power and temperature measurements could be provided from a MEMS (Micro-Electro-Mechanical) System chip [21]. But at the pressure and temperatures or primary conditions of this study – 200 bar and 400c – no MEMS chip would offer the necessary operating conditions. The mica heater was selected because it can survive the primary conditions of the $sCO_2$ tests. The mica heater is electrically powered by a Variable AC Voltage regulator or

(Variac). A wall outlet powers the variac. The variac allows for the voltage across the heater to be controlled. The mica heater is held in place by the backing plate screwed into the copper block, indicated by the threading at the bottom of the copper block in Figure 4.5. The mica heater supplies the heat flux, $q_{flux}$ to the block. The block is heated, so a temperature difference occurs between the impinging fluid and the block. The block's temperature is measured via three J-type thermocouples at locations 1, 2, and 3 in the figure below.

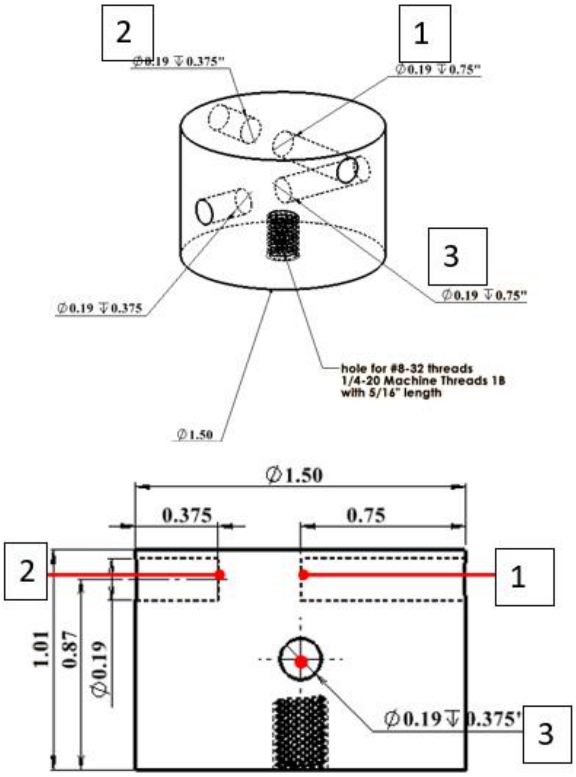

Figure 4.5: Thermocouples position within the copper block

The silicate holder, as shown in both Figure 4.1 and Figure 4.3, is used to hold the rest of the assembly and mitigate heat loss from the copper block since the material’s thermal conductivity is sufficiently low. Radial heat loss is further reduced by wrapping the assembly in an insulating ceramic sheet. This allows most of the heat to be transferred upward from the top surface with the impinging fluid. How the temperature of the surface is determined and the amount of heat loss is discussed in a later section.

## Rig Components

### *Bottom Flange Assembly*

Figure 4.6 shows the copper electrode gland fitting, allowing current from the variac to flow through the mica heater when the copper assembly is inside the pressure vessel. The thermocouples also have a gland fitting, shown in Figure 4.7, to feed the temperature readings outside the pressure vessel.

Figure 4.6: Copper electrode gland fitting

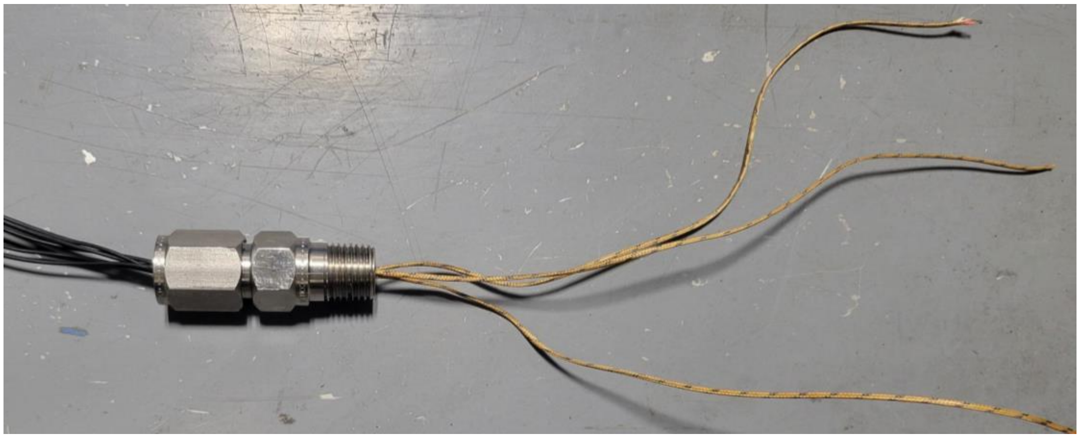

Figure 4.7: Thermocouple gland fitting

Figure 4.8 shows the copper block being instrumented with the thermocouples. This process involves potting each thermocouple hole shown in Figure 4.5 with thermal cement. Typically, a day is given to let each potted hole cure. All three gland fittings (two electrodes, one temperature) instrumented into the bottom flange are shown in Figure 4.9. Figure 4.10 shows the copper assembly instrumented with the thermocouples and mica heater wires connected to the copper electrode gland fittings and positioned at the center of the bottom flange.

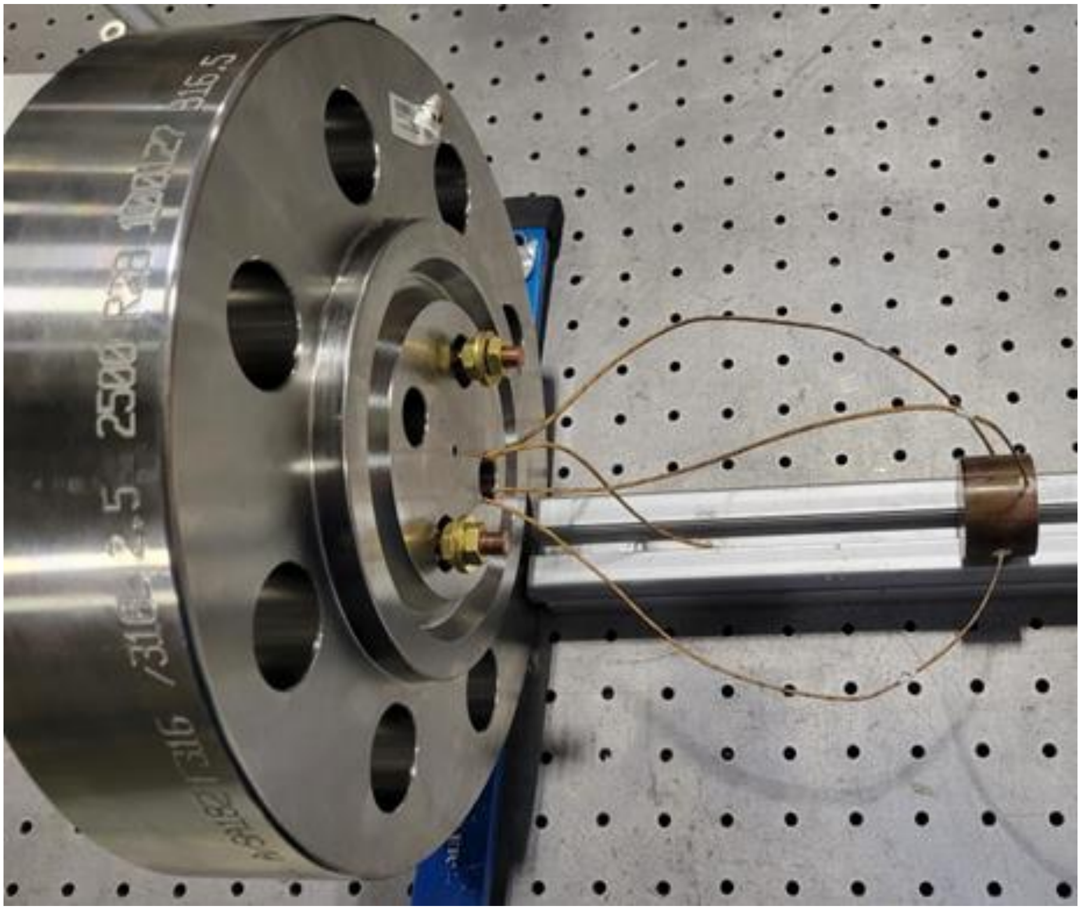

Figure 4.8: Copper block instrumentation

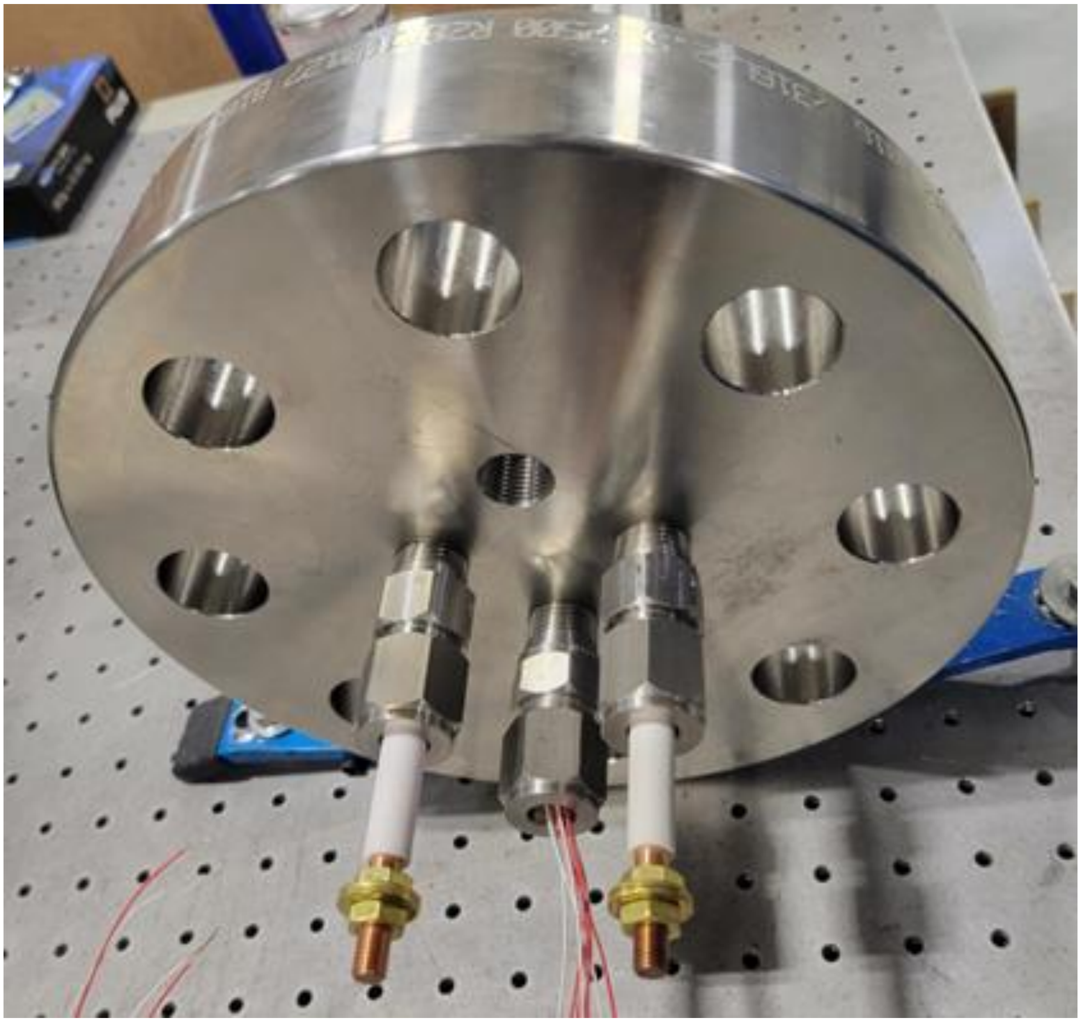

Figure 4.9: Gland fitting instrumentation

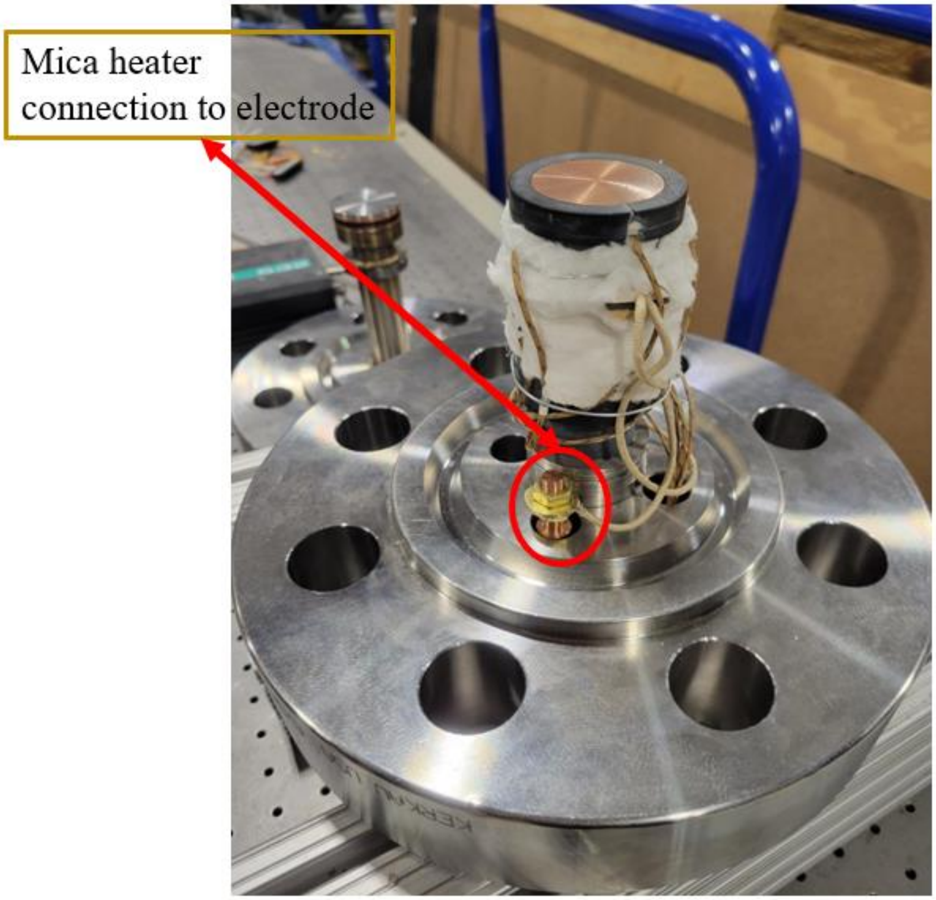

Figure 4.10: Bottom flange assembly

Figure 4.11 shows the copper block’s position inside the pressure vessel. Positioning the assembly inside the pressure vessel requires 3-4 people and can take 30-60 minutes. It’s a rather delicate procedure since the surface of the copper block needs to be normal to the flow, and if the assembly is not correctly placed within the pressure vessel, the surface could be at an angle. The surface’s alignment is checked visually through the openings at the side of the pressure vessel. The openings are closed by 2in NPT plugs. When attached to the bottom flange, the heat transfer setup is referred to as the bottom flange assembly shown in Figure 4.10.

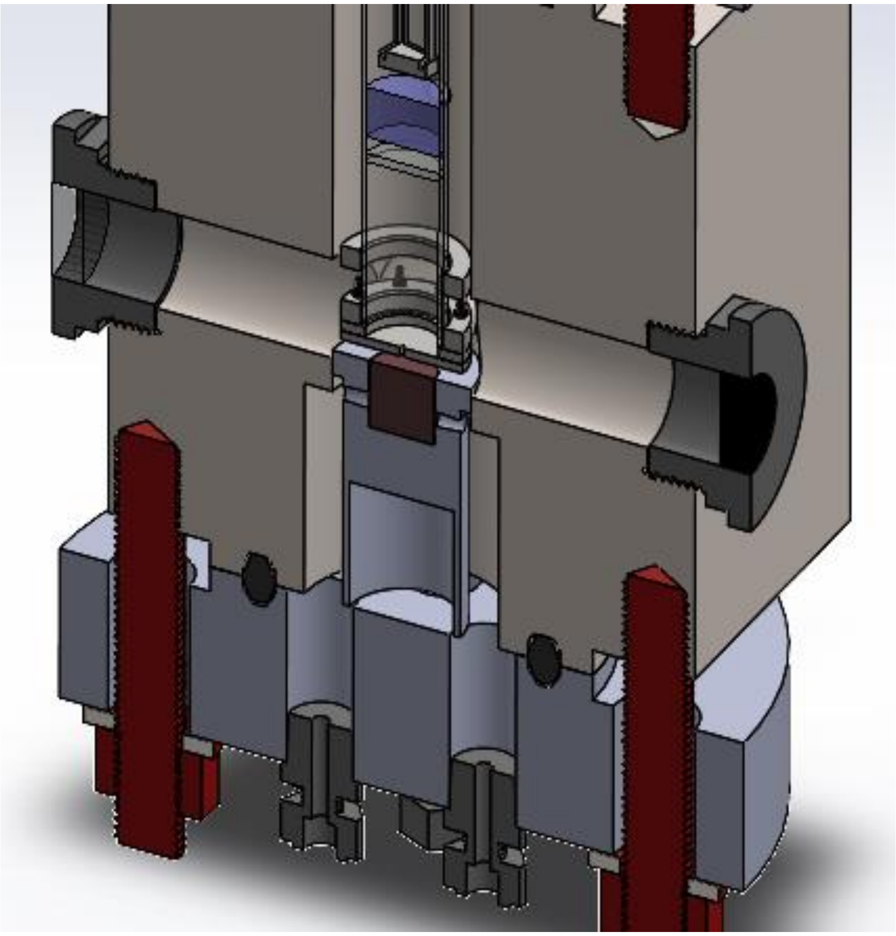

Figure 4.11: Copper block position in pressure vessel

*Top Flange Assembly*

The top flange assembly, Figure 4.12, consists of the top flange, deflector chamber, plenum, jet plate, and associated features. For the Rig air and $sCO_2$ test, the fluid travels through a quad fitting and the flange into the deflector chamber, where the fluid strikes the splash plate, diffuses through the deflector chamber openings into the plenum, and travels down to the jet plate. The purpose of the splash plate is to remove the flow energy associated with the pump so that the only driving force for the flow through the 3mm nozzle on the jet plate is pressure. The flow then impinges on the copper block and is driven up and out of the pressure vessel due to the pressure difference.

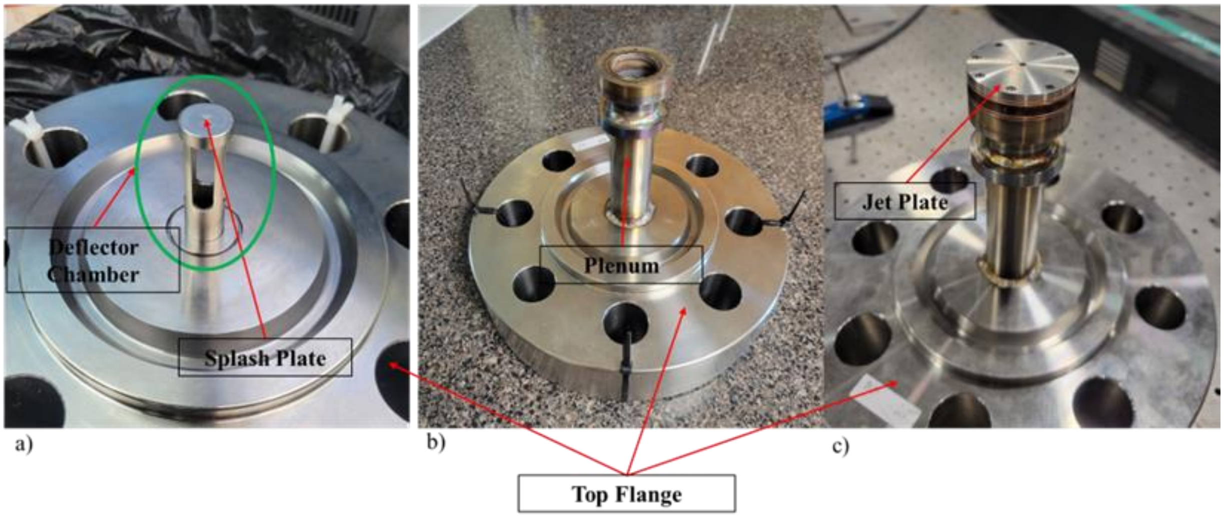

Figure 4.12:Top flange assembly a) Deflector chamber b) Plenum c) Jet plate

### *The Rig*

Figure 4.14 shows the fully assembled experimental apparatus, which will be referred to as the ‘Rig’ from this point onward. The Rig is composed of the top, and bottom flange assemblies instrumented onto the pressure vessel. A hydraulic torque wrench tightens the 1in bolts that fix the flanges onto the pressure vessel. An R28 soft iron RTJ gasket is wedged between the flanges to create a seal to prevent leaks. The groove where the gasket sits between the pressure vessel and the flanges is shown in Figure 4.13

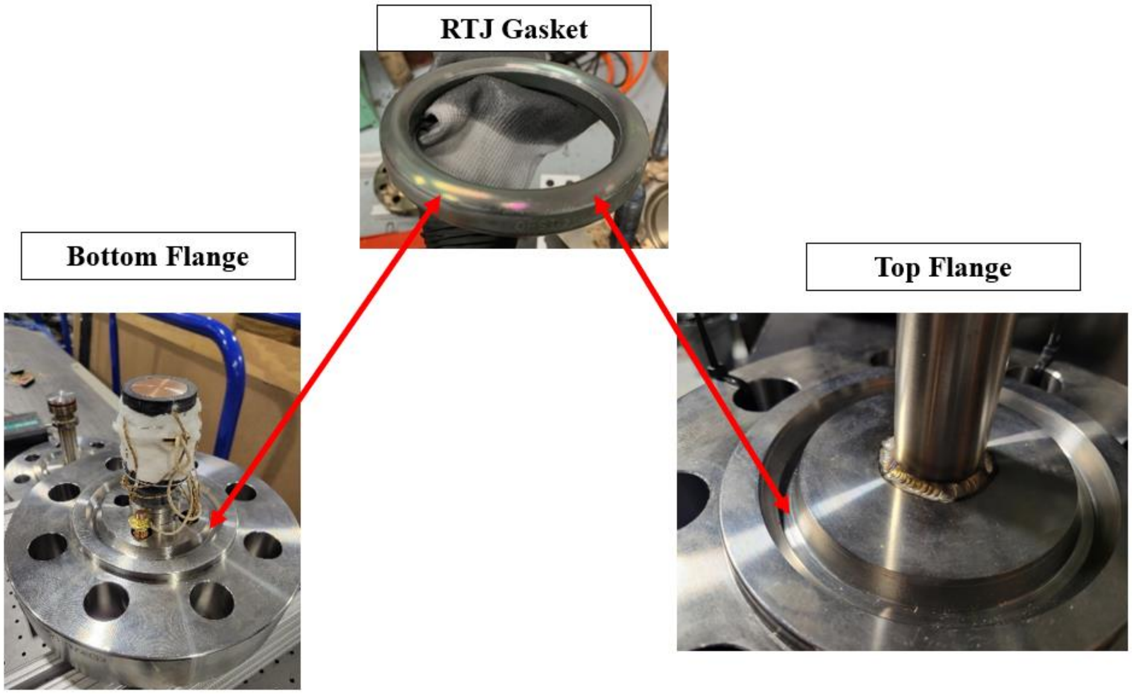

Figure 4.13: Gasket position between the flange and pressure vessel

Figure 4.14: Assembled Rig

## Air test in Rig setup

The benchtop and Rig air tests have essentially the same experimental setup. Air travels from the air compressor to the quad fitting, where pressure and temperature are measured, as shown in Figure 4.15, then impinges on the copper block surface. The needle valve regulates the mass flow measured using a mass flow sensor. The DAQ records the measured data. Figure 4.16 shows the Rig air test schematic. The air test verifies that the setup and procedures are correct by comparing the calculated Nusselt number to the correlation values. The correlations are discussed in the 'Air Validation' section.

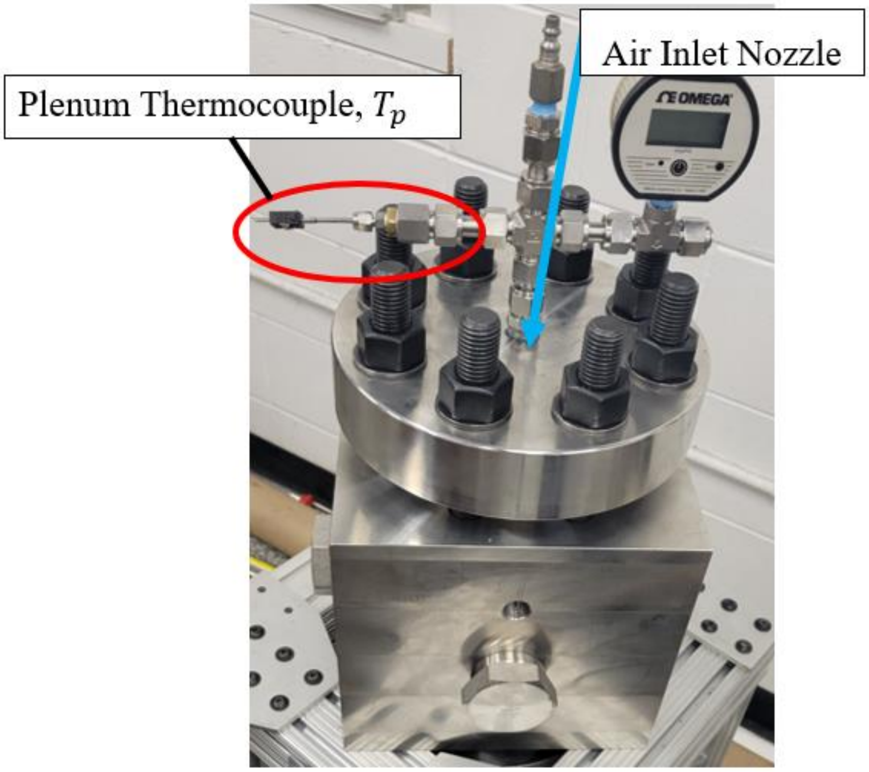

Figure 4.15: Thermocouple and air inlet positions

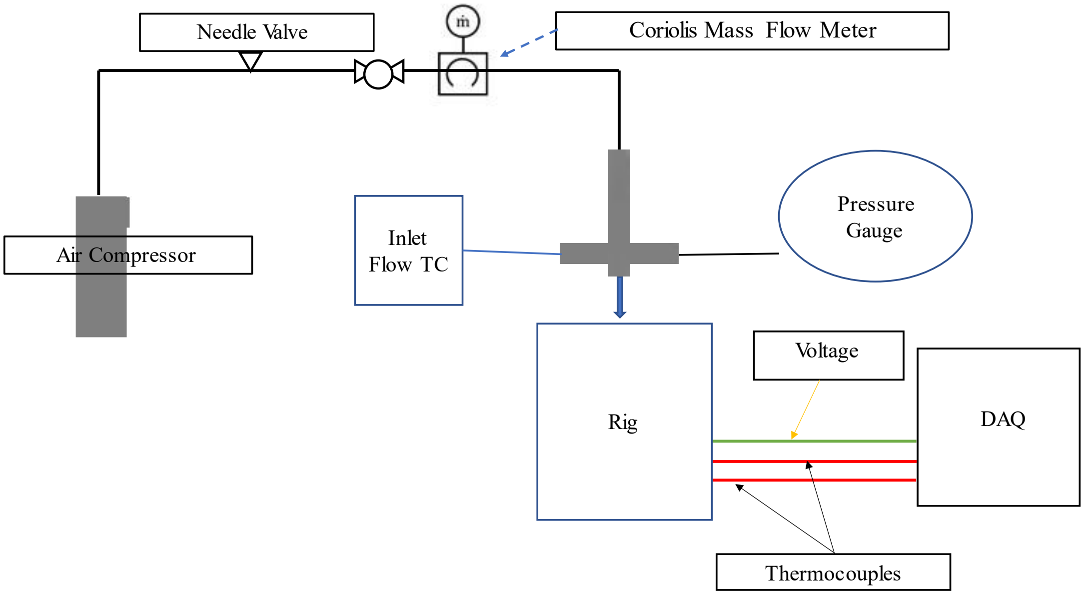

Figure 4.16: Rig air experiment setup

## Rig Integration

In Figure 4.17, you can see the Rig integrated into the $sCO_2$ experimental loop or simply the loop via the inlet pipe following the green lines into the quad fitting on top of the top flange. After impingement, the flow exits the Rig from the outlet piping, following the yellow arrows back to the loop. The loop consists of the components that generate, regulate, and heat the flow. The thermocouple in the normal position to the top flange measures the flow temperature into the plenum and is used to extrapolate the jet temperature; this process is discussed in the ‘Tare Data procedure.’ The Rig is insulated later to prevent more significant heat loss during the experiment with ceramic fiber with a thermal conductivity of 0.029 W/m/K.

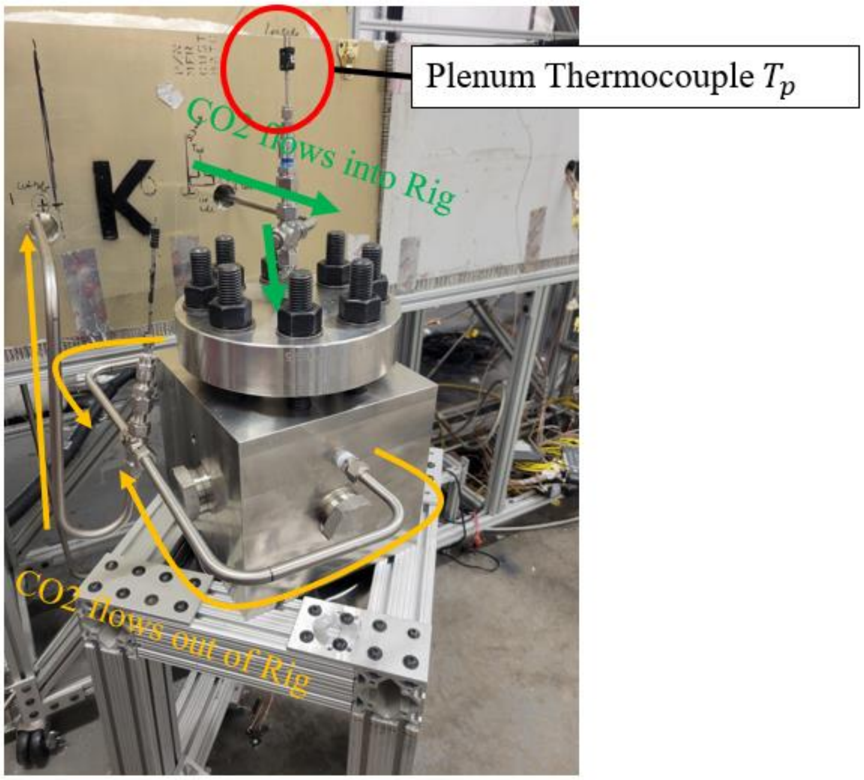

Figure 4.17: $CO_2$ flow path

## $sCO_2$ Experimental Loop

The figure below details the $sCO_2$ experimental loop referred to as the loop. The black arrow lines outline the mass flow path. The location where heating is applied is referred to as preheaters, the booster pump is where $CO_2$ is pumped into the system, and the jet impingement experiment is located after the busbar power supply section, where additional heat is added to the flow. The test facility where the system is located is equipped with a ventilation system that quickly removes any leaked $CO_2$ to outside the room. $CO_2$ concentration sensors are also located throughout the room and notify experimenters if the concentration exceeds 1000 ppm.

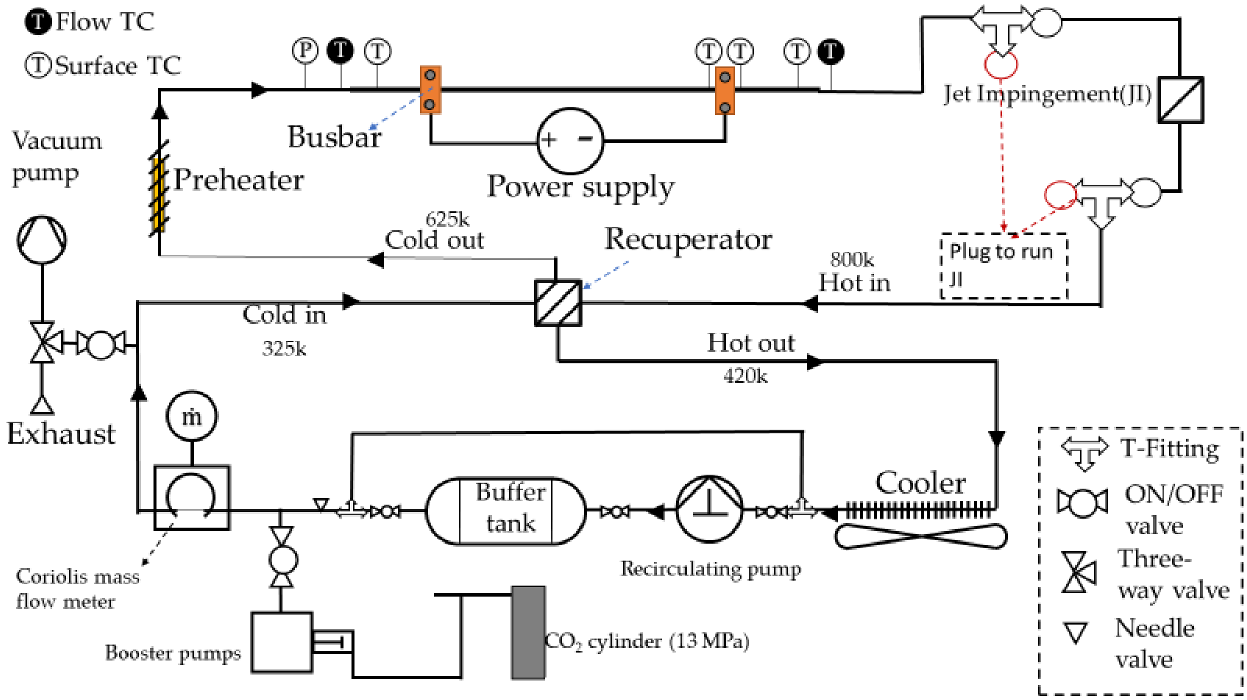

Figure 4.18: $sCO_2$ experimental loop

## $sCO_2$ Test Procedure

This section will discuss the $sCO_2$ loop components and the procedures; a brief overview of each step in the procedure is outlined below:

Step 1: Pressurization

Step 2: Initial Steady State

Step 3: Tare Data Procedure

Step 4: Maintain Conditions

Step 5: Cool Down

Step 6: Depressurize

### *1st pressurizing phase*

Before the test begins, the loop is vacuumed, removing any air or nitrogen in the loop. While running these experiments, only $CO_2$ should be in the lines, and the purity of the $CO_2$ in the cylinders is 99.9%. To begin, the valve at location 2 in Figure 4.19 is open, and the loop depressurizes to atmospheric conditions. Then the pump at location 1 is connected to the loop, turned on, and the loop begins to approach vacuum conditions of approximately -30psi. Once a sufficient vacuum has been established, the valve at location 2 is closed, and the vacuum pump is turned off.

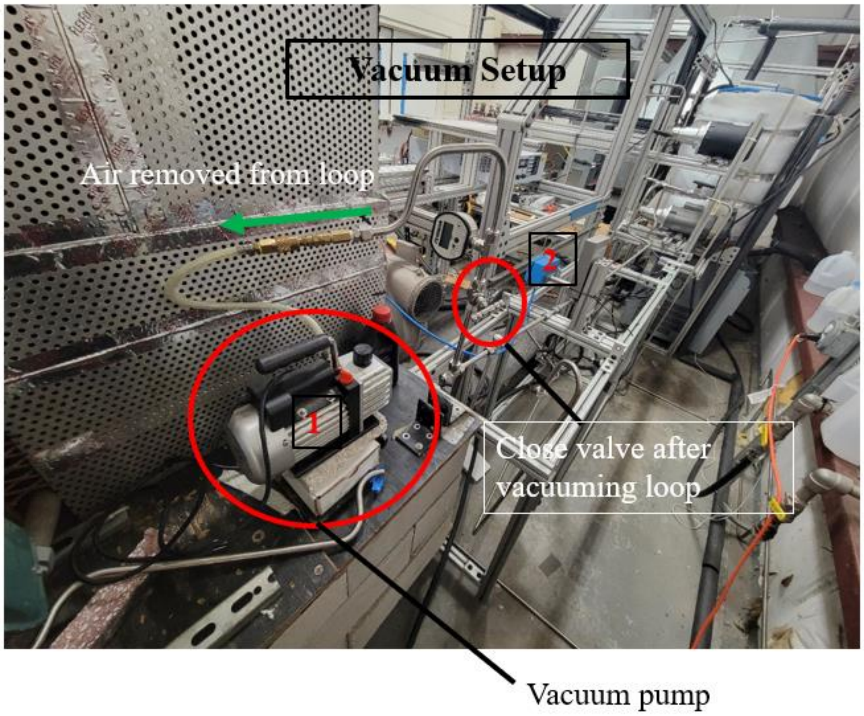

Figure 4.19: Vacuum setup

The next step is pressuring the loop by opening the valves around the buffer tank and recirculating the pump, labeled as a, b, and c in Figure 4.20. This will increase the pressure in the loop to around 40-55 bar. The goal is to get the pressure to 200 bar. Afterward, the recirculating pump is turned on at the operating panel to get the flow going in the loop. This flow will be tuned to the desired flow rate as the value will change throughout the experiment due to changing conditions like temperature and pressure.

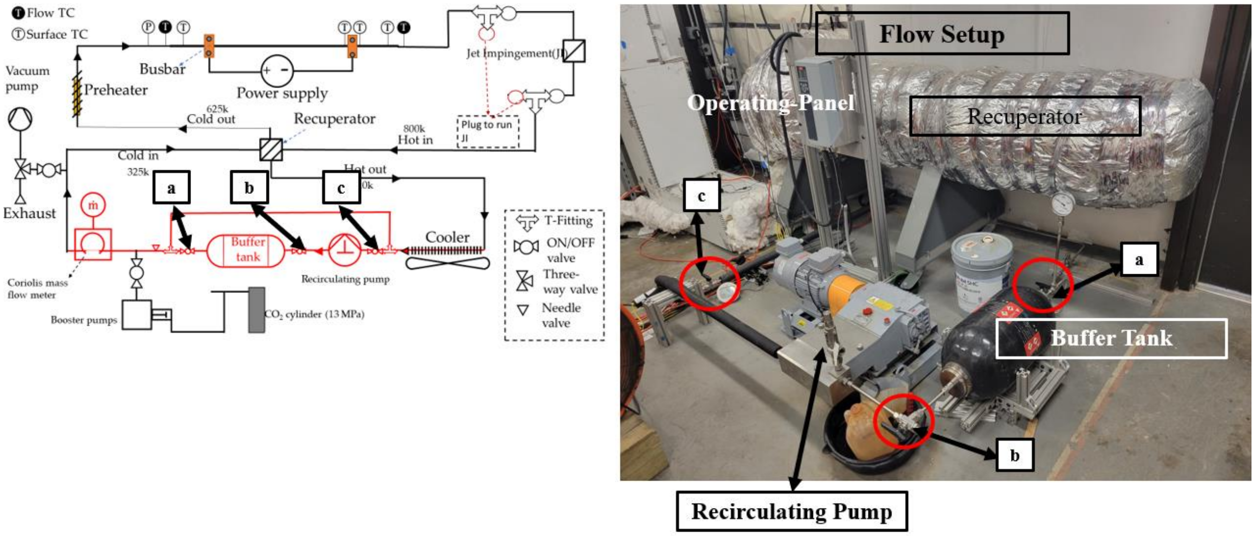

Figure 4.20: Mass flow setup

The components for cooling the loop are also turned on; these components are for keeping the temperature of the $CO_2$ in the recirculation pump within its operating range. The water cooler valve is opened; first, this allows the water in the water drum, shown in Figure 4.21, to flow through the heater exchangers, circled in green. The hot $CO_2$ transfers heat with the water in the drum. The water from the drum transfers heat with cold water from the chiller, also shown in Figure 4.21, within the heat exchangers. The drum water keeps the $CO_2$ entering the circulating pump within its operating conditions, and the chiller keeps the drum water temperature low. The cooling system is a closed loop, the water from the drum will return to the drum after exiting the heat exchanger, and the water from the chiller will return to the chiller after leaving the heat exchanger. The temperature of the room will impact the performance of the chiller.

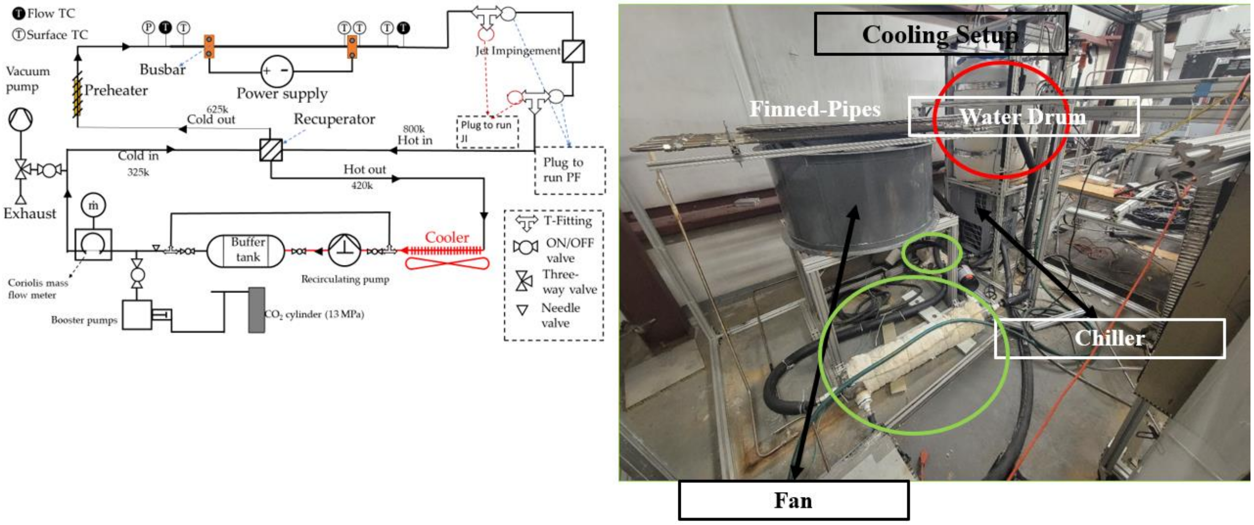

Figure 4.21: Cooling system setup

For adding more $CO_2$ into the loop, we use two booster pumps in series that pump $CO_2$ from the cylinders to the loop shown in Figure 4.22. At location 1 in Figure 4.22, the cylinder is open, allowing $CO_2$ to flow into the loop along the green line. The pumps are driven by compressed air, which is permitted to flow into the pumps when the valve at location 2 is open. The loop is pressurized between 130-150 bar before the number 2 valve is closed to turn the booster pumps off, and then the number 1 valve is shut off to seal the cylinders. The loop is also isolated from the booster pumps via an on-off valve that is closed to allow the booster pump lines to be vented and detached from the loop and the cylinders. These pumps are then moved and attached to the recuperator and nitrogen cylinders to fill the recuperator shell.

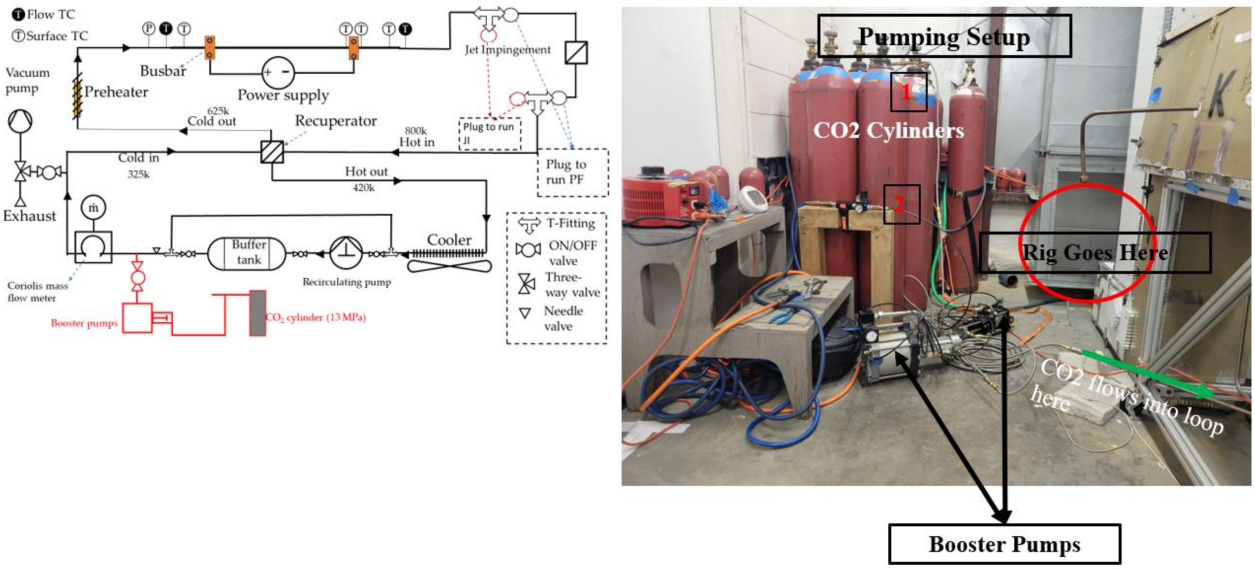

Figure 4.22: Pressurizing setup

Heat is added to the flow using fifteen rope heaters along the yellow and red lines. Eight variacs regulate the power distributed to the rope heaters. The busbar section is composed of a DC power supply with two positive and negative terminals. A pair of copper wires connect to the terminals of a DC power supply, which also connect to the loop via nickel busbars, providing a voltage difference that heats the stainless-steel pipe, thus heating the flow. The heat flow setup is shown in Figure 4.23. Experimenters try to use the busbar section sparingly due to maintenance requirements from damages discussed in the ‘Rig Operation Challenges’ section.

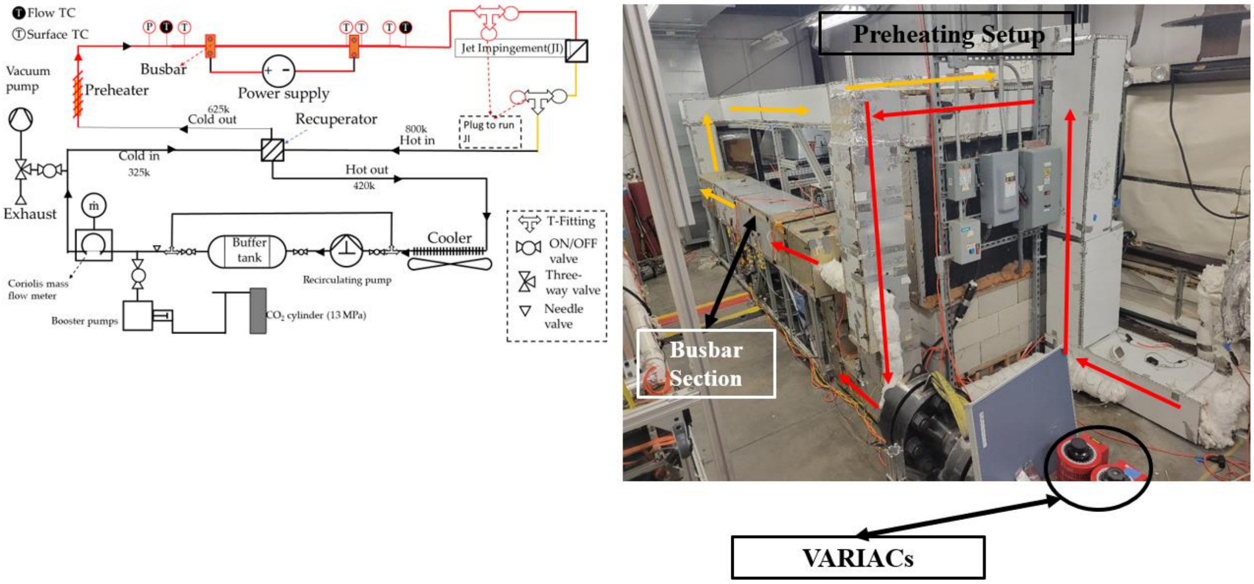

Figure 4.23: Heating setup

As the flow is heated, the recuperator shell is filled with nitrogen. Nitrogen is used due to its affordability. Figure 4.24 shows that nitrogen is pumped into the shell from ‘Start’ to ‘Finish.’ The shell is pressurized between 90-120 bar. Due to a loose fitting in the shell, it is necessary to pressurize the recuperator to reduce $CO_2$ leaking from the loop into the shell. In addition, the recuperator allows for waste heat from the outlet of the experiment to be reused to heat the incoming flow back into the experiment. This can be seen as the ‘Hot in’ line, which is the outlet of the experiment exchanging heat with the ‘Cold in’ line, coming from the recirculating pump in Figure 4.24.

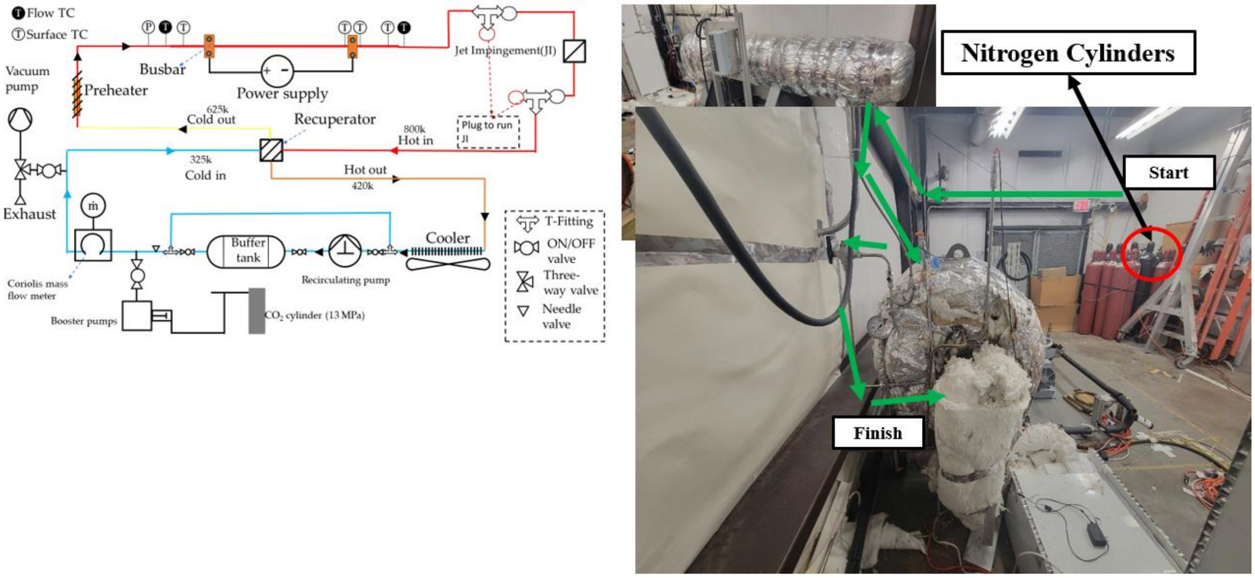

Figure 4.24: Nitrogen flow path to the recuperator

*2nd pressurizing phase*

Once the recuperator shell is pressurized until about 120 bar, the shell is isolated from the nitrogen cylinders. The booster pumps are disconnected and moved to be attached to the $CO_2$ cylinders. The pumps are then reattached to the $CO_2$ cylinders, and the loop is further boosted with $CO_2$ until aroound 225 bar. The target pressure value is overshot because of pressure leaks and the time it takes for the loop to reach steady conditions at the Rig and recuperator. The mass flow rate required to meet the Reynolds number for each test is calculated using the intended test conditions – typically 200 bar at 400c – on an excel spreadsheet. The flow rate is monitored and adjusted using the loop's recirculating pump and two other valves. Also, during each test, whether or not the transmitter's flow rate and DAQ match must be verified. The two instruments match up to the hundredth place for all experiments. The next section covers the 'Tare Data procedure,' beginning with a general discussion about the goal of this process.

### *Tare Data procedure*

By the time the tare data procedure is being performed, the mass flow and pressure are in acceptable ranges: Mass flow rate is steady at about an average value, and pressure is above 210 bar. An example of steady-state conditions for obtaining the tare data is shown in Figure 4.25. The main concern is to obtain the correct jet temperature.

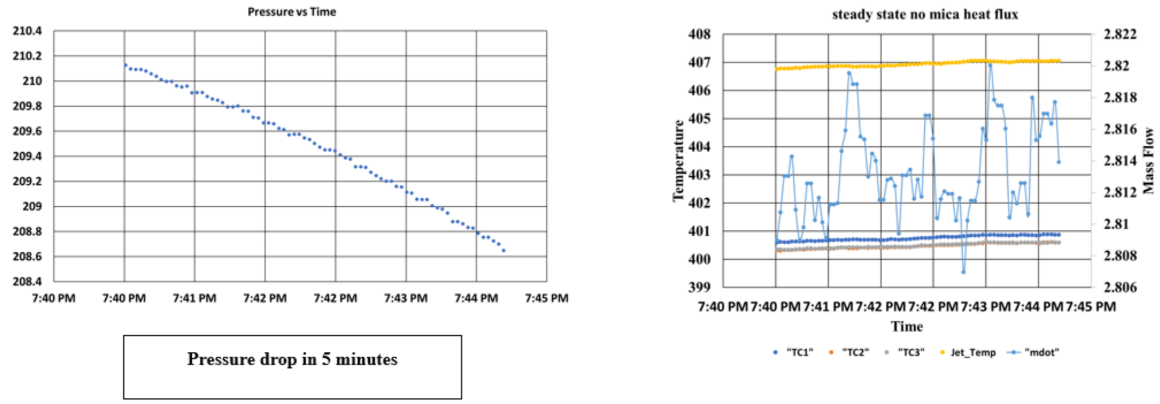

Figure 4.25: Steady pressure, mass flow, and temperature conditions

## The Ideal Case

The goal is to measure the jet temperature impinging on the copper block. Figure 4.26a shows that the flow temperature can be obtained at two locations if no heat flux is applied. The thermocouple at the plenum inlet, $T_p$ and $T_s$ at the copper block. In this case, the temperature at the plenum and block would be the same as shown in Figure 4.26a when no heat flux is applied. When a heat flux is applied, the block $T_s$ increases and cannot be used to represent the jet temperature, shown in Figure 4.26b, but this is fine as the plenum temperature accurately represents the jet temperature.

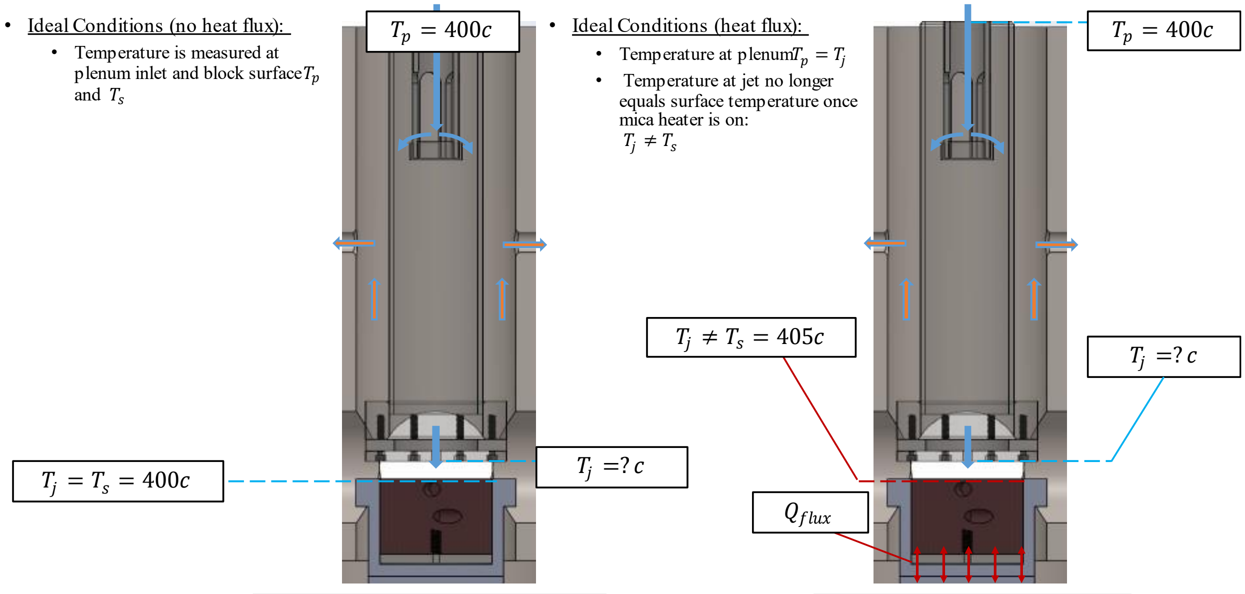

a: sCO2 Experimental setup w/ no heat flux

b: sCO2 Experimental setup w/ heat flux

Figure 4.26: Ideal conditions: a) no heat flux, b) with heat flux

## The Actual Case

In the actual case, heat is lost from $T_p$ to $T_s$, as shown in Figure 4.27a. By the time the flow reaches the copper surface, it is no longer 400c, meaning the jet temperature condition for the test is no longer met, and there is a temperature difference or dT between the plenum and the surface shown. To account for the heat loss, more heat is inputted into the flow until the copper block temperature is at 400c. But now, only the block temperature accurately represents the jet temperature at the primary conditions, as the plenum temperature is higher. This would mean once the mica heater is turned on and a heat flux is applied to the block, the means to measure the jet temperature would be lost. To avoid this, the temperature difference between the plenum and block before the heater is turned on is used to obtain the jet temperature. In Figure 4.27a, you can see the setup when no heat flux is applied to the block. The temperature difference is simply $T_p$-$T_s$. In Figure 4.27b, the heater is on, and the block temperature can no longer represent the jet temperature. To get the jet temperature, dT is subtracted from $T_p$. This is the tare data procedure.

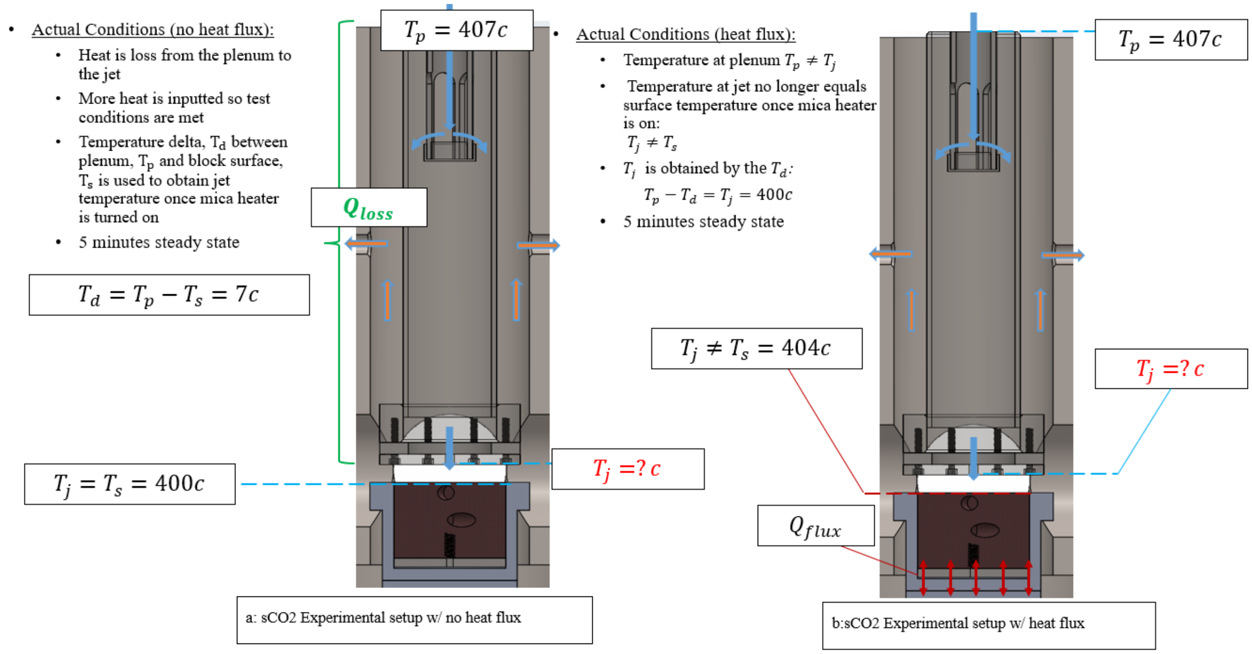

a: sCO2 Experimental setup w/ no heat flux

b:sCO2 Experimental setup w/ heat flux

Figure 4.27: Actual conditions: a) no heat flux, b) with heat flux

During experiments, this would mean collecting 5 minutes of data while the experiment matches the no heat flux conditions and then collecting 5 minutes of data while the experiment matches heat flux conditions. At either of these stages in the experiment, the mass flow and pressure conditions must also be maintained, or the tare data procedure will have to be redone. Due to leaks in the loop, pressure drops significantly, applying a time constraint on both stages of the experiment. If pressure dropped too low, more $CO_2$ would have to be pumped into the loop; steady-state conditions must be obtained again, and the tare data procedure must be restarted. It can take somewhere between 20-60 minutes to regain stable values before beginning the tare data procedure again. Figure 4.28a show’s the time history of pressure and mass flow during one experiment. In addition, Figure 4.28b shows the time history for a cool-down process for concluding an experiment. A test’s total time can be between 8-12 hours.

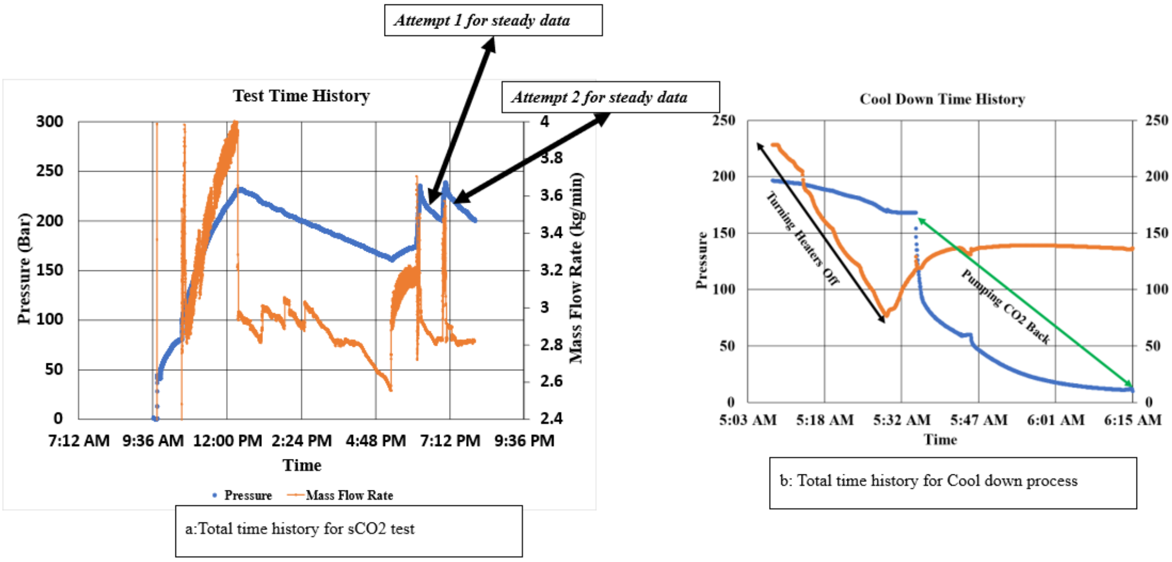

a:Total time history for sCO2 test

b: Total time history for Cool down process

Figure 4.28: Time history plots: a) total test time b) total cool down time

### *Rig Operation Challenges*

There is a lot more involved in the Rig test vs. the benchtop test. This is because tests need to operate under much more extreme conditions. The conditions are somewhere between 200 and 250 bar and 400 and 500c. All components inside the pressure vessels must survive these conditions for multiple tests. We also have to contain this pressure; this means that the flanges, 2in NPTs, fittings, and gland fittings must be able to sustain this. For the flange, this means torquing the bolts down to 4000 psi, which compresses the gasket allowing for a seal between the flange and the top and bottom of the pressure vessel. This is also done incrementally in four passes following a tightening sequence. The 2in NPTs, fittings, and gland fittings are tightened following assembly standards. Whether or not the fittings are correctly tightened is assessed during a pressure test where the Rig and loop are filled with $CO_2$ and leaked tested as the pressure increases incrementally. To leak test means experimenters use a specialized liquid to coat the fittings and pressure-sealed locations on the Rig and loop; if bubbles form, there is a leak. Leaks indicate the loop must be depressurized and fittings adjusted and tightened. Fittings are replaced if they don't seal the leak after adjustment and tightening. For the $sCO_2$ test, a properly tightened down Rig means none of the fittings are leaking. This can also depend on whether or not the fittings have also experienced the 400c temperatures, which can damage the fittings and require them to be tightened more or replaced.

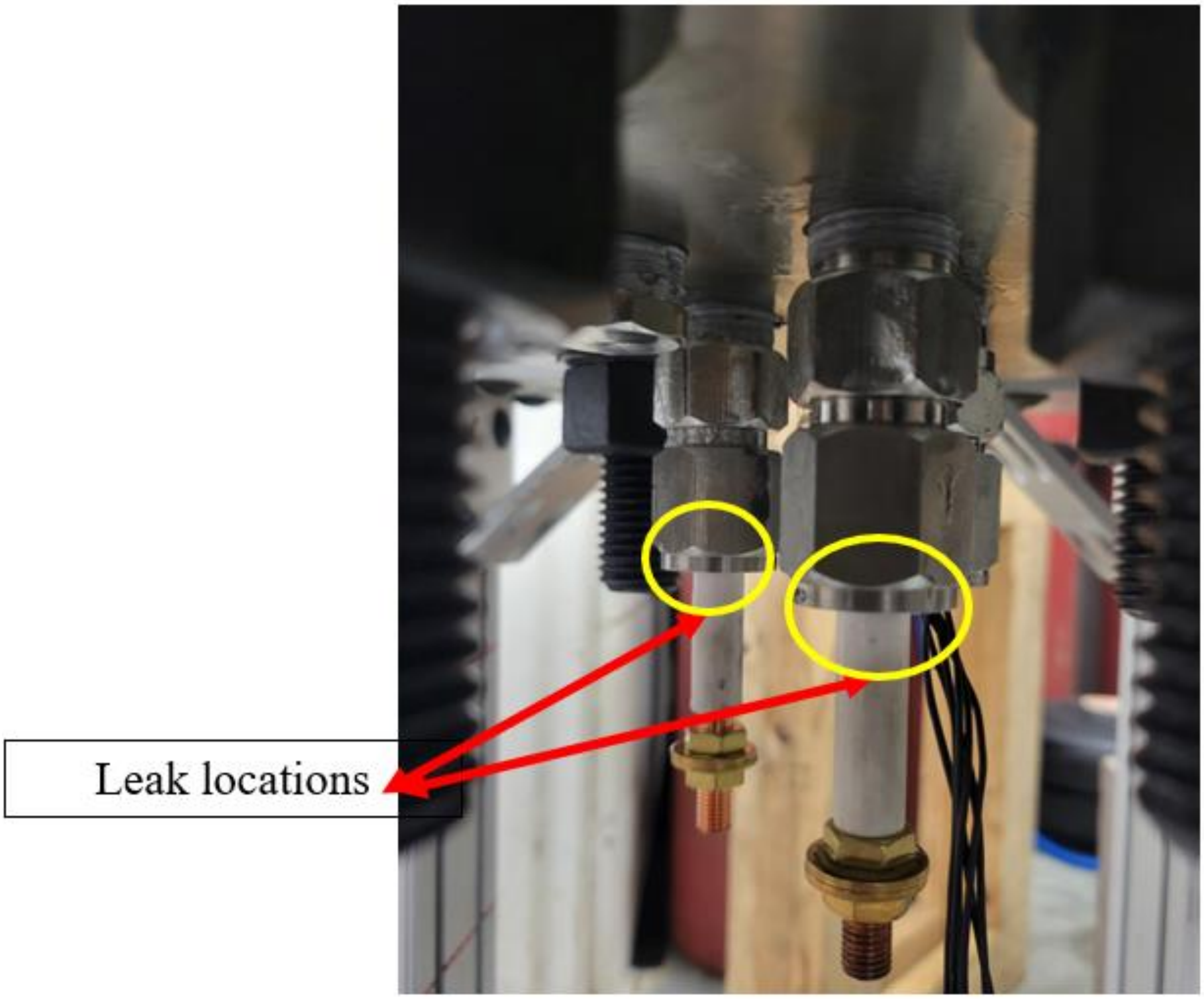

Figure 4.29: Gland fitting leaks

Unfortunately, a couple of the gland fittings were not adequately sealed when manufactured and would leak throughout the test, as shown in Figure 4.29. In addition, after completing all the tests, it was determined that the torque wrench for the flange was not correctly assembled, and the amount of torque that was calculated to be applied was not the actual amount. This is the most likely contributor to why gasket failures occurred. An additional problem occurs when the DC power supply is used to heat the flow. A pair of copper wires connected to the terminals of a DC power supply and to the loop via nickel busbars provides a voltage difference that heats the stainless-steel pipe and, in turn, heats the flow. These copper wires oxidate and then shear apart, cutting off the heat supply to the flow. This will reduce the temperature of the flow, and temperature conditions for the test cannot be reached until this damage is repaired. Two separate instances of damaged busbar wires are shown in Figure 4.30. Figure 4.31 shows the complete timeline of $sCO_2$ experiments and images of experimenters assessing a gasket failure.

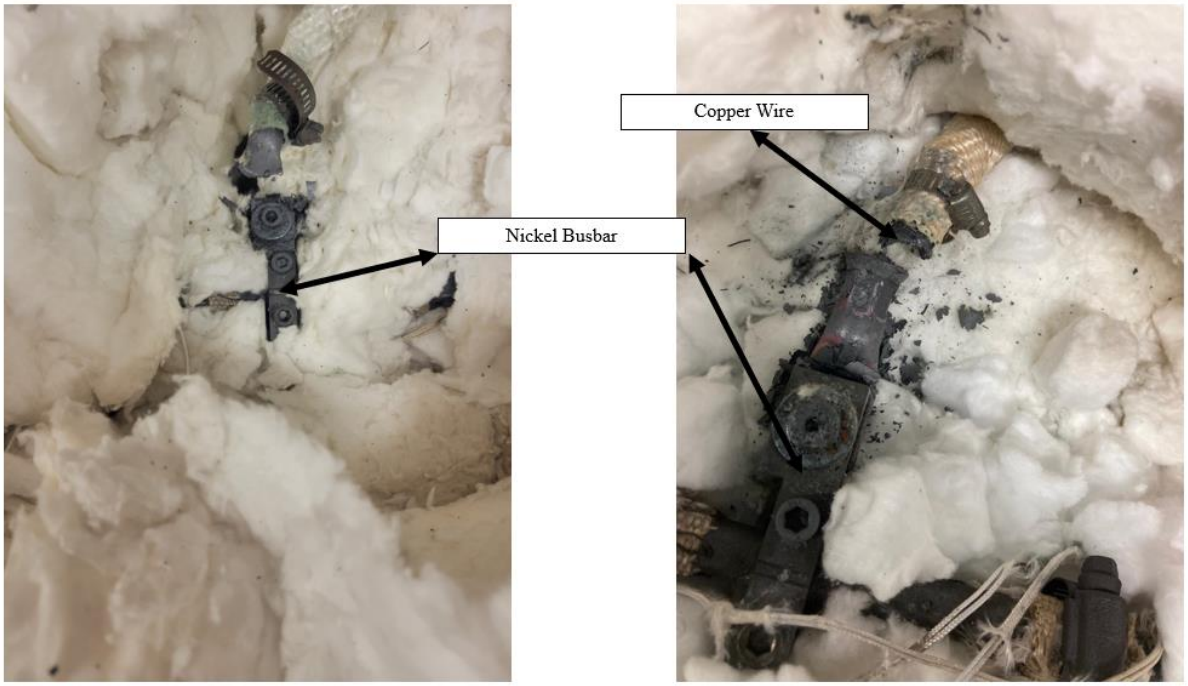

Figure 4.30: Busbar damage

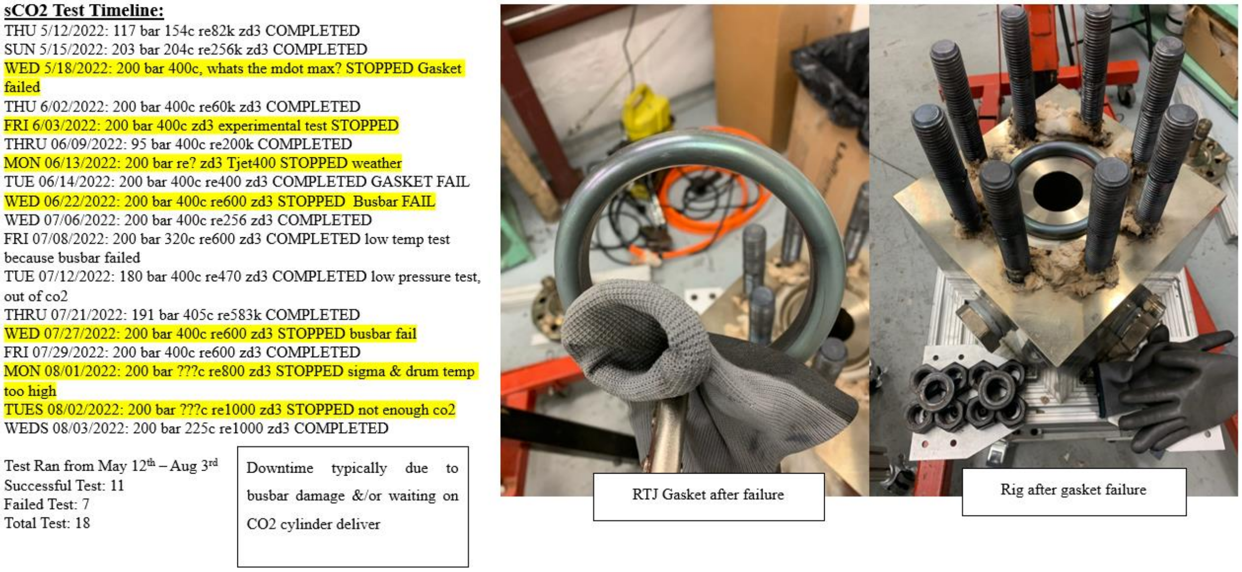

**sCO2 Test Timeline:**

THU 5/12/2022: 117 bar 154c re82k zd3 COMPLETED
SUN 5/15/2022: 203 bar 204c re256k zd3 COMPLETED
WED 5/18/2022: 200 bar 400c, whats the mdot max? STOPPED Gasket failed
THU 6/02/2022: 200 bar 400c re60k zd3 COMPLETED
FRI 6/03/2022: 200 bar 400c zd3 experimental test STOPPED
THRU 06/09/2022: 95 bar 400c re200k COMPLETED
MON 06/13/2022: 200 bar re? zd3 Tjet400 STOPPED weather
TUE 06/14/2022: 200 bar 400c re400 zd3 COMPLETED GASKET FAIL
WED 06/22/2022: 200 bar 400c re600 zd3 STOPPED Busbar FAIL
WED 07/06/2022: 200 bar 400c re256 zd3 COMPLETED
FRI 07/08/2022: 200 bar 320c re600 zd3 COMPLETED low temp test because busbar failed
TUE 07/12/2022: 180 bar 400c re470 zd3 COMPLETED low pressure test, out of co2
THRU 07/21/2022: 191 bar 405c re583k COMPLETED
WED 07/27/2022: 200 bar 400c re600 zd3 STOPPED busbar fail
FRI 07/29/2022: 200 bar 400c re600 zd3 COMPLETED
MON 08/01/2022: 200 bar ???c re800 zd3 STOPPED sigma & drum temp too high
TUES 08/02/2022: 200 bar ???c re1000 zd3 STOPPED not enough co2
WEDS 08/03/2022: 200 bar 225c re1000 zd3 COMPLETED

Test Ran from May 12th – Aug 3rd
Successful Test: 11
Failed Test: 7
Total Test: 18

Downtime typically due to busbar damage &/or waiting on CO2 cylinder deliver

RTJ Gasket after failure

Rig after gasket failure

Figure 4.31: $sCO_2$ total test timeline

## Surface Temperature Calculation

This section will discuss how the surface temperature of the copper block is determined. Figure 4.32 shows the position of the thermocouples used during testing. The copper block has a 1in height, and thermocouples 1 and 2 are at a z-position 0.87in up from the bottom of the copper block. Thermocouple 1 is positioned directly under the stagnation point; this means it is centered within the block. Thermocouple 2 is at an R-position between the center and outer radius of the block. The third thermocouple is at the same R-position as the first but 0.51in up vertically from the bottom surface. The fourth position is not used.

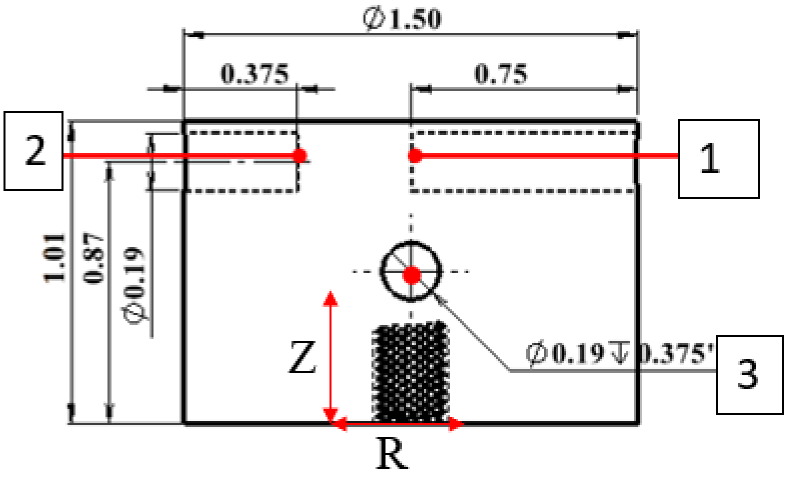

Figure 4.32: Thermocouple positions

For data analysis, temperature and mass flow are at steady conditions, constant heat flux is applied, and no heat is generated from within the copper block. An example of 5 minutes of steady conditions is shown in Figure 4.33.

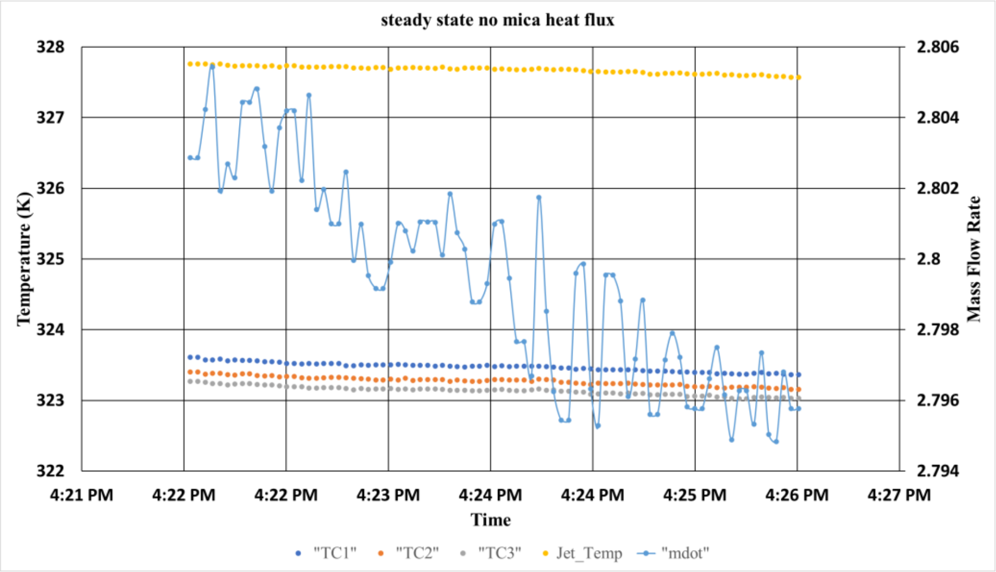

Figure 4.33: Steady conditions, no heat flux

The equation for determining the temperature at the surface is shown in Figure 4.34. When x = 1in the temperature of the surface of the copper block, $T_s$ is determined. This linearly extrapolated temperature is obtained from the three thermocouples discussed.

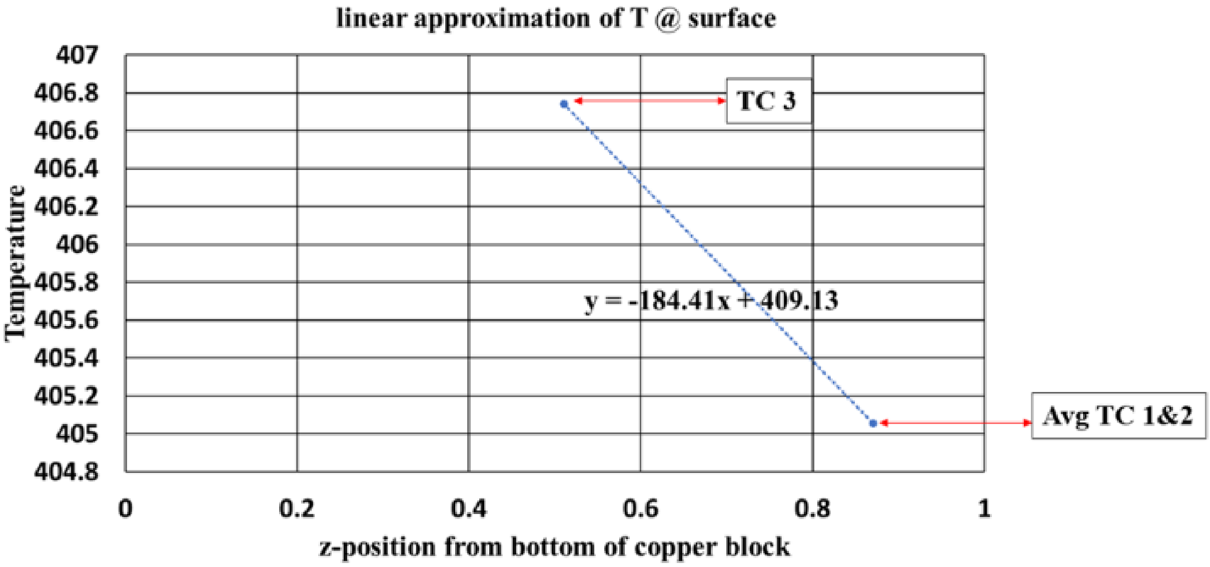

Figure 4.34: Plot used to determine the surface temperature

### Heat Loss Test

Figure 4.35 shows the setup for the heat loss experiments. The only difference between this setup and the one shown in the copper block assembly in Figure 4.4 is that now a Rohacell block, with a thermal conductivity of 0.02 W/m/K, is placed on the top surface of the block. This test aims to quantify how much heat will be lost to the area surrounding the copper block during the test with flow. The heat loss experiments setup and methodology are the same for the benchtop and Rig tests.

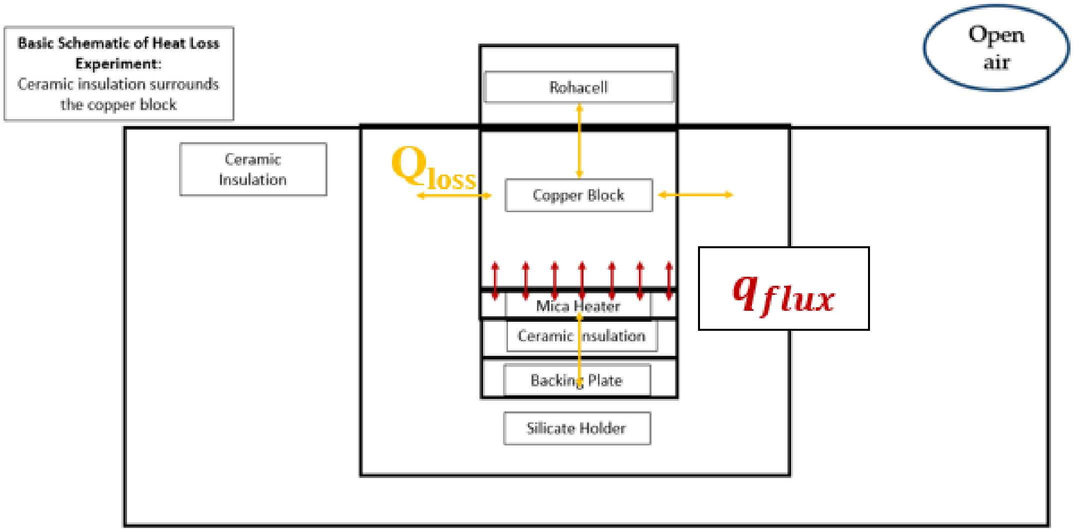

Figure 4.35: Heat loss experiment setup

As shown in equation 4.2, all the heat supplied is equal to the $Q_{loss}$, whereas, during the test shown in Figure 4.4 and equation 4.1, the heat will also be transferred with the fluid as well.

$$q_{flux} = q_{flux} \times A = Q_{supply} = Q_{convection} + Q_{loss} \tag{4.1}$$

$$Q_{supply} = \frac{V^2}{R} = Q_{loss} \tag{4.2}$$

The mica heater is supplied with a voltage to obtain a specific block temperature. Then, room temperature is subtracted from the measured blocked temperature to determine the temperature delta.

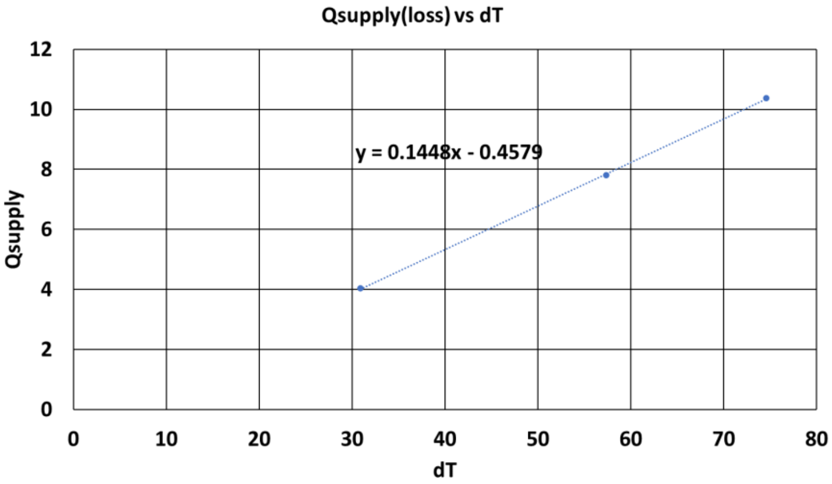

Figure 4.36: 3-point heat loss test

Once a steady state is reached, meaning the thermocouple temperatures are no longer changing for at least 10 minutes, the test at that specific block temperature is complete and referred to as one point on the heat loss line. Then the voltage is increased to get the next point at a higher dT. Figure 4.36 shows the 3-point (pt) heat loss test that was performed for the benchtop tests. Figure 4.37 shows the 4-pt heat loss test that was performed for the Rig tests. The relationship established is that $Q_{supply}$ or $Q_{loss}$ on the y-axis has a linear relationship with dT. The linear equation is used to approximate the heat loss during the experiments.

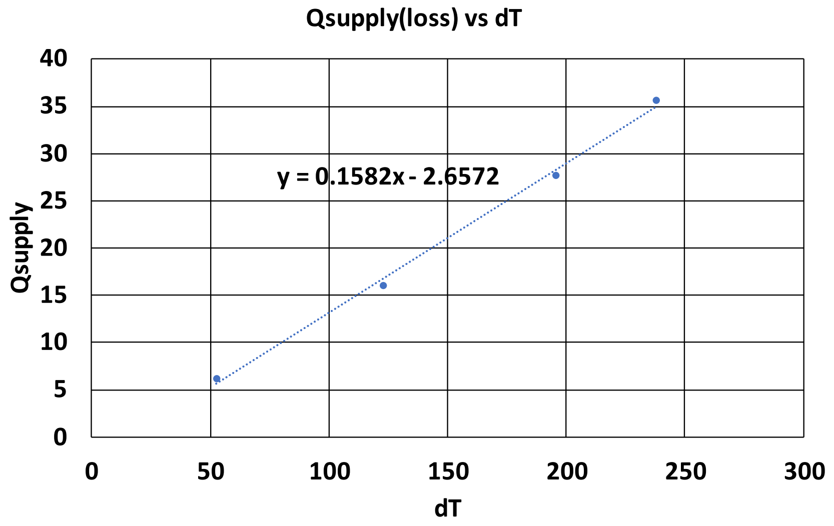

Figure 4.37: 4-point heat loss test

Data Reduction

The area of the cross-section for the jet nozzle is calculated using equation 4.3.

$$A_{jet} = \pi {r_{jet}}^2 \tag{4.3}$$

Similarly, the surface area of the impinging surface is determined by the following:

$$A_S = \pi {r_S}^2 \tag{4.4}$$

Supply power for heating the copper block is calculated using the voltage from the mica heater and the resistance across it.

$$Q_s = \frac{V^2}{R} \tag{4.5}$$

As discussed in the 'Heat Loss Test' section, the heat loss is defined using the following equation:

$$Q_l = m \times dT + b \tag{4.6}$$

Using supply power, heat loss, area of the impinging surface, and temperature difference between the jet and the impinging surface, the heat transfer coefficient can be determined:

$$h = \frac{Q_s - Q_l}{A_S \times dT} \tag{4.7}$$

The non-dimensional heat transfer coefficient, Nusselt number, is calculated using the heat transfer coefficient, jet diameter, and fluid property thermal conductivity, k. The thermal conductivity is determined by CoolProp using temperature and pressure values from the experiment:

$$Nu = \frac{h \times D_j}{k} \tag{4.8}$$

## Uncertainty Analysis

The method used to determine the propagation of uncertainty in the analysis is described in the Test Uncertainty Standard PTC 19.1-2005 by the American Society of Mechanical Engineers (ASME) [31]. The relative expanded uncertainties in measured parameters for air and $CO_2$ are shown in Tables 4.2 and 4.3. As suggested by the National Institute of Standards and Technology (NIST), the uncertainty in thermophysical properties from CoolProp are neglected [32]. Nusselt number is not included in Table 4.3 due to the significant deviation per test. Nusselt number uncertainty for the $sCO_2$ test is shown in Figure 5.11 in the '$sCO_2$ Results' section. Figure 4.38 shows the propagation of uncertainty through relevant parameters. Equation 4.9 is the general equation for determining uncertainty. The absolute expanded uncertainty is $u_\alpha$; alpha is the independent variable. The sensitivity coefficient is theta; i is each dependent variable, and n is the last dependent variable. The absolute combined standard uncertainty for the i dependent variable is $u_i$. Table 4.1 shows the independent variables and dependent variables. The propagation of uncertainty in the heat transfer coefficient is determined by inputting $Q_s$, $Q_l$, $D_{surf}$, and dT into equation 4.9 as the independent variables.

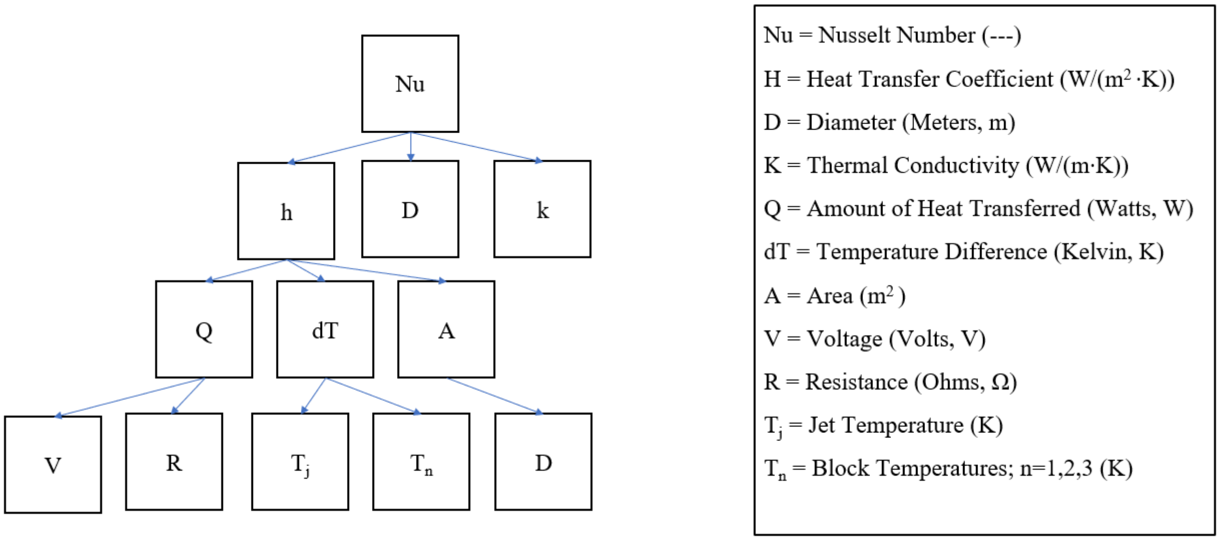

Nu = Nusselt Number (---)
H = Heat Transfer Coefficient (W/(m$^2$·K))
D = Diameter (Meters, m)
K = Thermal Conductivity (W/(m·K))
Q = Amount of Heat Transferred (Watts, W)
dT = Temperature Difference (Kelvin, K)
A = Area (m$^2$)
V = Voltage (Volts, V)
R = Resistance (Ohms, Ω)
$T_j$ = Jet Temperature (K)
$T_n$ = Block Temperatures; n=1,2,3 (K)

Figure 4.38: Error propagation tree

$$u_\alpha = \sqrt{\sum_{i=1}^{n} (\theta_i u_i)^2} \tag{4.9}$$

Table 4.1: Independent variables and dependent variables

| **α** | **i** |
|---|---|
| Nu | h, Dj |
| h | $Q_l$, $Q_s$, $D_{surf}$, dT |
| $Q_l$ | dT |
| $Q_s$ | V, R |

Table 4.2: Air test uncertainties

| **Parameter Uncertainties at each Reynolds Number for Air** | | | |
|---|---|---|---|
| **Re** | **100** | **60** | **25** |
| Nusselt Number | 20% | 20% | 23% |
| Jet Pressure | 0.5% | 0.8% | 1.36% |
| Temperatures | 2.2C | 2.2C | 2.2C |
| Mass Flow Rates | 0.5% | 1% | 3% |
| Resistance | 14% | 14% | 14% |
| Voltage | 5% | 5% | 5% |

Table 4.3: $CO_2$ test measure parameters uncertainty

| **Parameter Uncertainties at each Reynolds Number for $CO_2$** | | | |
|---|---|---|---|
| | **Maximum** | **Minimum** | **Average** |
| Jet Pressure | 2.0% | 0.5% | 1.00% |
| Temperatures | 2.2C | 2.2C | 2.2C |
| Mass Flow Rates | 0.4% | 0.1% | 0.2% |
| Resistance | 14% | 14% | 14% |
| Voltage | 5% | 5% | 5% |

# CHAPTER 5: RESULTS AND DISCUSSION

In order to determine if the results obtained in the Rig are correct, the experimental setup is first validated with air cases. The experimental Nusselt number should be within a reasonable deviation of the correlations. The correlations used are shown in Table 5.1, with the coefficients for the required correlations below in Table 5.2. The experimental Nusselt number is determined from equation 4.8 in the 'Data Reduction' section.

Table 5.1: Air correlation

| **Author** | **Reynolds Number** | **H/D** | **R/D** | **Correlation** |
|---|---|---|---|---|
| Martin [27] | 2,000-400,000 | 2-12 | 2.5-7.5 | $Nu_{avg} = Pr^{0.42}\frac{D}{r}\frac{1-1.1D/r}{1+0.1\left(\frac{H}{D}-6\right)D/r}ARe^{n}$ |
| Huang [28] | 6,000-124,000 | 1-10 | 0-10 | $Nu_{avg} = Pr^{0.42}Re^{0.76}[a+bH+cH^2]$ |
| Sagot [29] | 10,000-30,000 | 2-6 | 3-10 | $Nu_{avg} = 0.0623Re^{0.8}\left[1-0.168\left(\frac{R}{D}\right)+0.008\left(\frac{R}{D}\right)^2\right]\left(\frac{H}{D}\right)^{-0.037}$ |
| Goldstein [30] | 61,000-124,000 | 6-12 | --- | $\frac{24-\left\lvert\frac{H}{D}-7.75\right\rvert}{533+44\left(\frac{R}{D}\right)^{1.394}}Re^{0.76}$ |

Table 5.2: Air correlation coefficients

| **Author** | **Coefficients** |
|---|---|
| Martin | for 2,000 < Re < 30,000, A = 1.36, n = 0.574<br>for 30,000 < Re < 120,000, A = 0.54, n = 0.667<br>for 120,000 < Re < 400,000, A = 0.151, n = 0.775 |
| Huang | $a = 10^{-4}[506 + 13.3R - 19.6R^2 + 2.41R^3 - 9.04 \times 10^{-2}R^4]$<br>$b = 10^{-4}[32 - 24.3R + 6.53R^2 - 0.694R^3 + 2.57 \times 10^{-2}R^4]$<br>$c = -3.85 \times 10^{-4}[1.147 + R]^{-0.0904}$ |

## Air Validation

The validation tests are the benchtop and Rig air tests. These tests were done to validate the heat transfer methodology, data reduction, and data acquisition systems. After performing the air test and obtaining results matching air correlations, the Rig $sCO_2$ test was performed. The experimental conditions for the benchtop, Rig air, and $sCO_2$ test are shown below:

**Experimental Test Conditions:**
R/D = 6.35
Air
- H/D = 2, 3, 6, 8 (Benchtop)
- H/D = 3, 7.4 (Rig)
- Reynolds Number = $25 \times 10^3 - 100 \times 10^3$
- Target dT ≈50c

$sCO_2$
- H/D = 2.8
- Reynolds Number = $82 \times 10^3 - 1,000 \times 10^3$
- Target dT=large as possible

The benchtop test is the first validation test. The test is of a free, unconfined impinging jet; thus, confinement is not an issue impacting the experimental Nusselt number. The benchtop test consists of 4 different H/Ds: 2,3,6,8. The Reynolds number range consisted of 25,000, 60,000, and 100,000. Figure 5.1 shows the Benchtop test for H/D = 2 with the experimental Nusselt number shown as diamonds and the correlations as different colored circles. This is consistent throughout all Nusselt number vs. Reynolds numbers plots. The accuracy of the benchtop tests is maintained for H/D's 3,6 and 8, shown in figures 5.2,5.3, and 5.4. This demonstrates that the heat transfer methodology, data reduction, and data acquisition systems are being properly carried out. Though the conditions of these tests are turbulent, Figure 5.5 shows that within the H/D range tested, the Nusselt number change remained relatively small, as demonstrated by Brdlik and Savin, whose tests were conducted under laminar conditions[19].

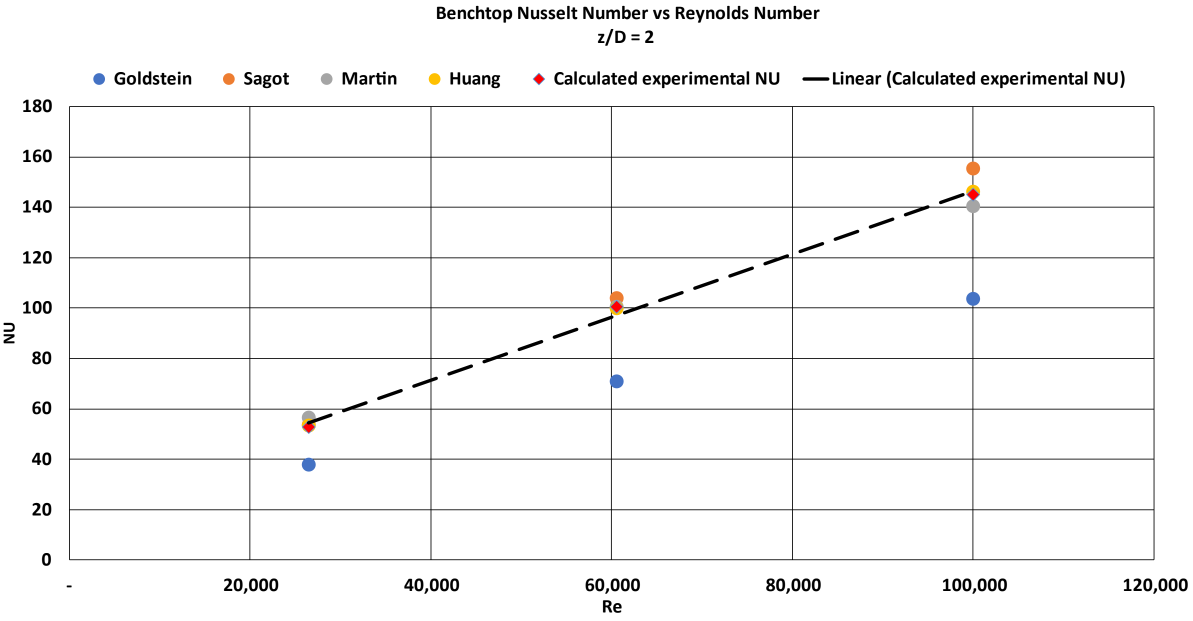

Figure 5.1: Air Benchtop Test Results z/D= 2

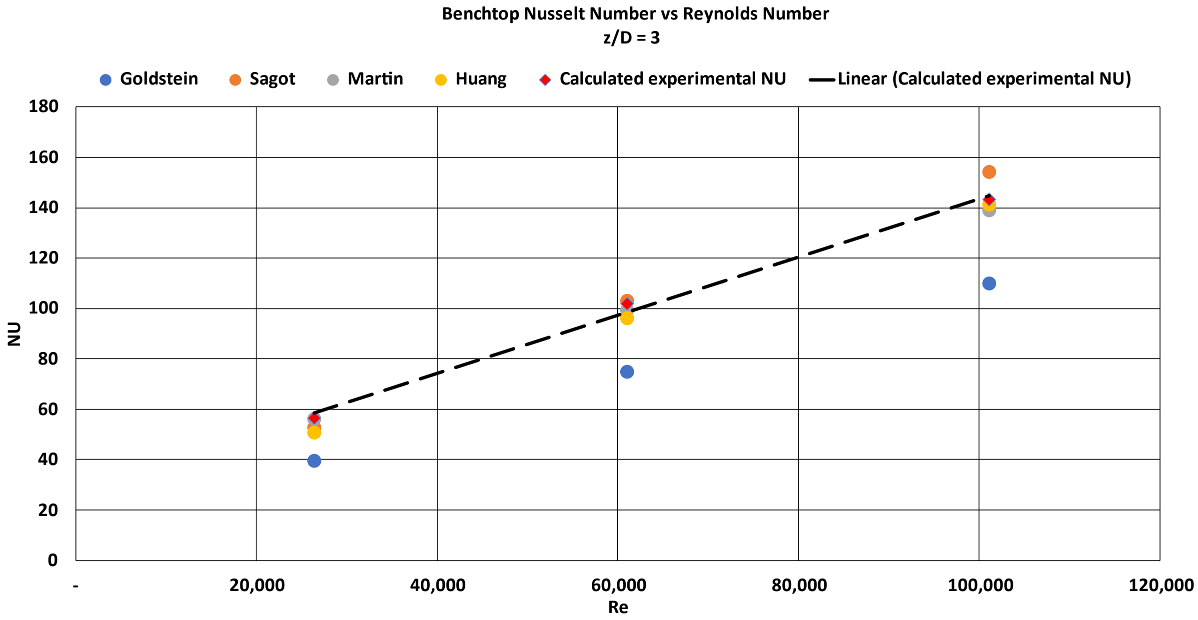

Figure 5.2: Air Benchtop Test Results z/D= 3

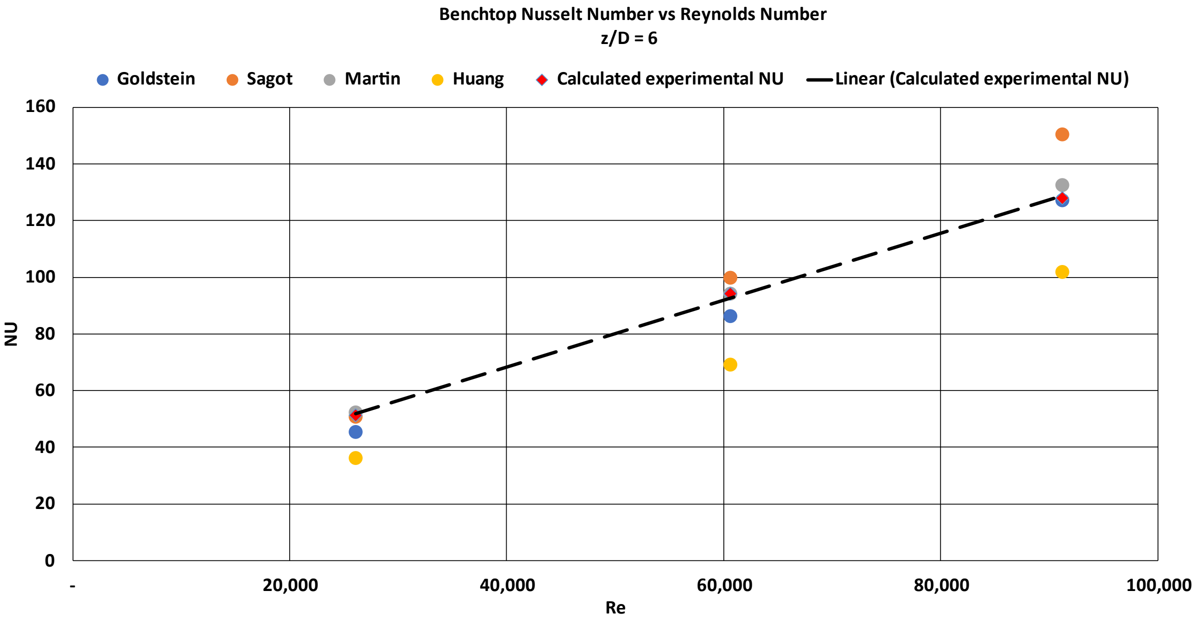

Figure 5.3: Air Benchtop Test Results z/D= 6

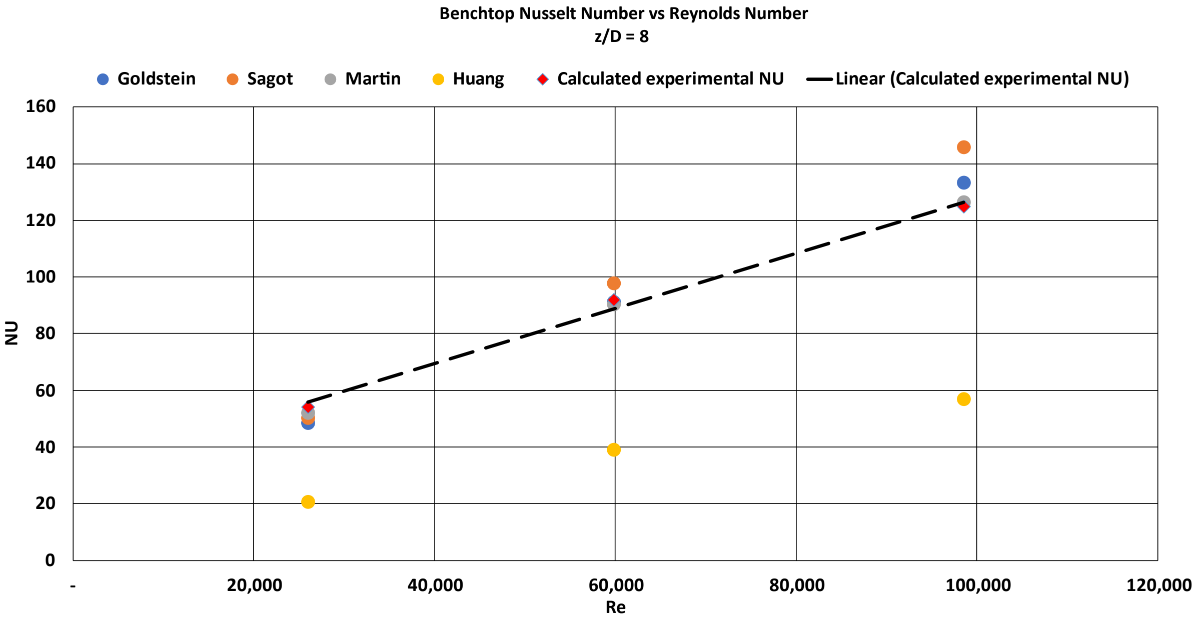

Figure 5.4: Air Benchtop Test Results z/D= 8

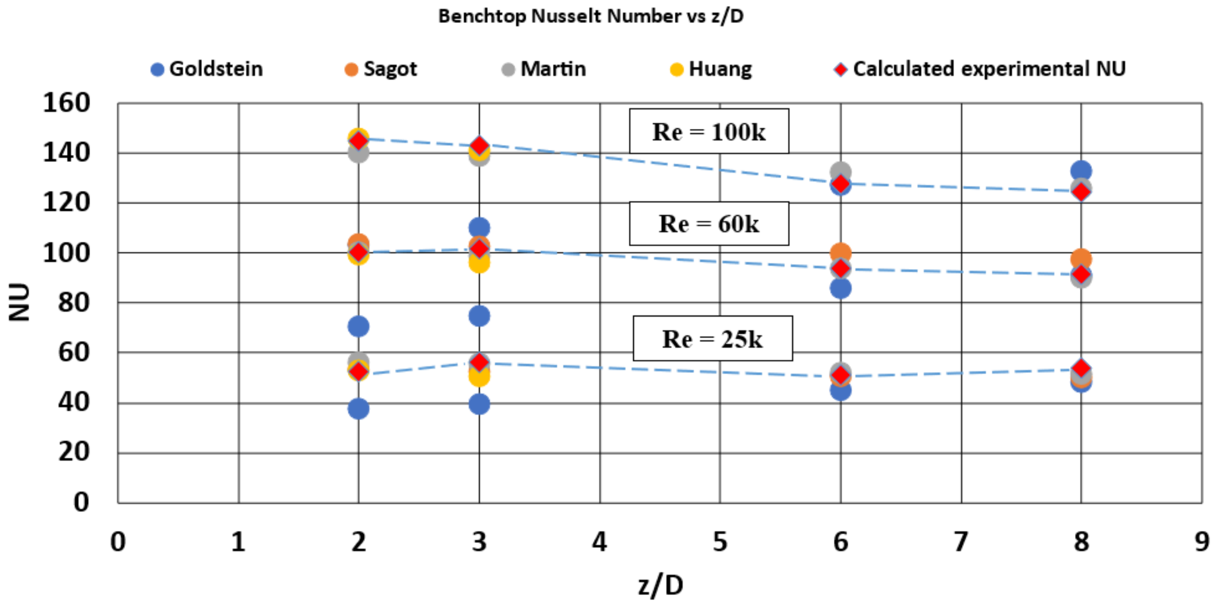

Figure 5.5: Air Benchtop Test Nu vs z/D, follows similar trend shown by laminar cases

The second validation test is performed in the Rig. Figure 5.6 shows the cluster of tests per Reynolds number. The Reynolds number range is the same as the Benchtop test. Seven tests were performed for the H/D =3 case. CFD cases, shown as orange squares in Figure 5.6, were run for specific cases with Reynolds Numbers of 26,810, 61,669, and 100,508. Mesh independence for each case was established. The maximum deviation from the average Nusselt number at each Reynolds Number from lowest to highest is 4%, 8%, and 7%. Shown in Figure 5.7 are the two tests for the H/D=7.4, a secondary validation case.

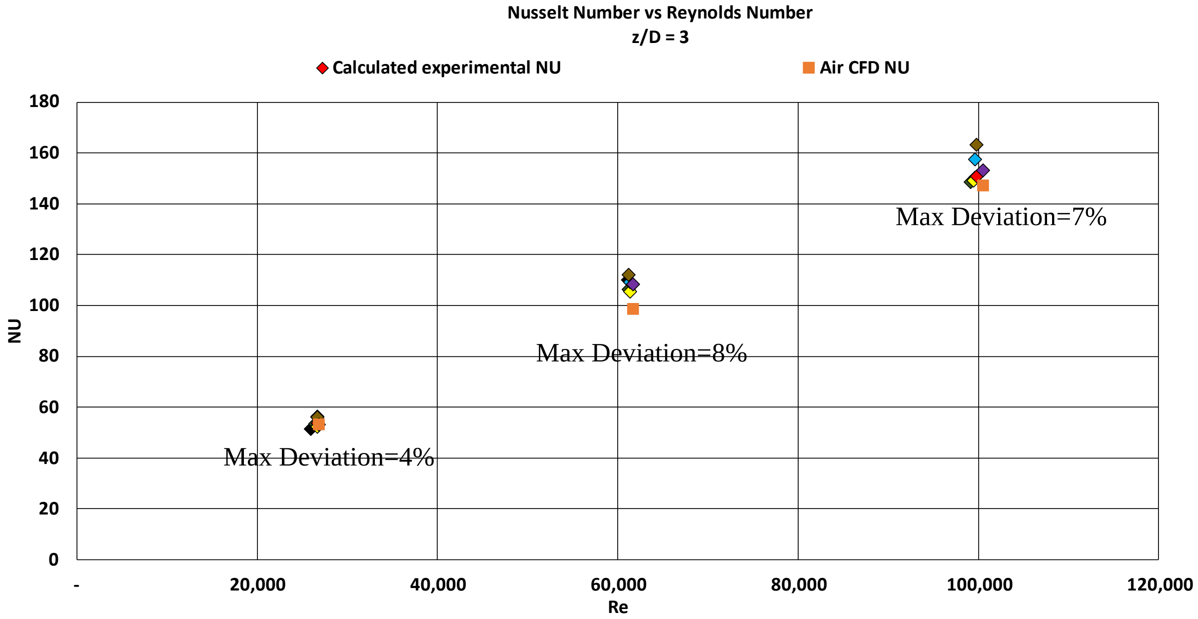

Figure 5.6: Experimental Rig Results w/air for z/D = 3 without Correlations, Max deviation of experimental data from average also shown

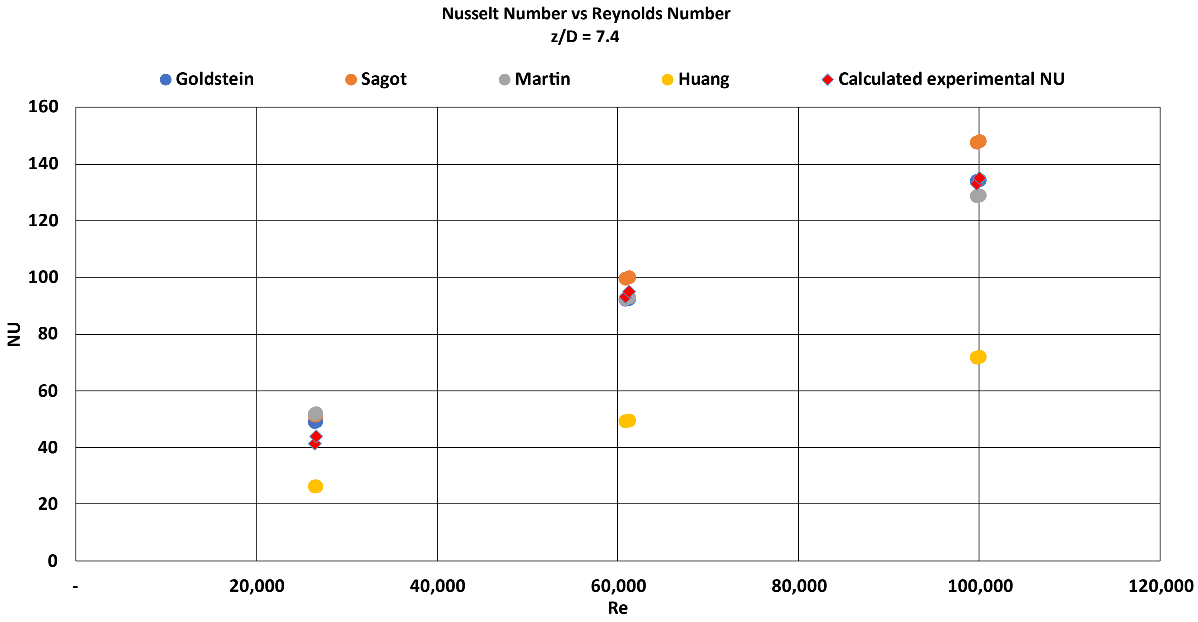

Figure 5.7: Air Rig Test Results z/D= 7.4

## sCO$_2$ Results

In Table 5.3, starting from the 194 bar test, begins the test that either meets or are close enough to be comparable to the experimental goals or primary conditions, i.e., jet temperature and pressure of 400c and 200 bar. The primary condition is to maintain the jet temperature of 400c. All the tests in Figure 5.8 met this condition. Only two tests, one at 95 bar and another at 179 bar, are not at the intended pressure condition. Observing these two tests in Figure 5.8, both test results have a little deviation from the trend line. The test that was at 95 bar has a 6% deviation, and the 179 bar test has a 1% deviation.

Table 5.3: $sCO_2$ Test Conditions with dT

| **P, T** | **Reynolds number** | **dT** |
|---|---|---|
| 117 bar 154c | 82,932 | 53.47 |
| 203 bar 204c | 256,147 | 15.04 |
| 197 bar 225c | 1,157,380 | 2.60 |
| 203 bar 320c | 638,993 | 3.16 |
| 194 bar 413c | 105,092 | 8.53 |
| 95 bar 412c | 197,393 | 10.63 |
| 209 bar 416c | 249,984 | 7.69 |
| 197 bar 415c | 401,103 | 5.16 |
| 179 bar 413c | 470,112 | 4.85 |
| 191 bar 405c | 583,443 | 4.18 |
| 202 bar 400c | 601,530 | 4.01 |

Additionally, a significant discrepancy is shown between the air correlations and the experimental $sCO_2$ Nusselt numbers. This lack of agreement between the data set and the correlations shows that the air correlations cannot be used to determine the Nusselt number for $sCO_2$ jet impingement. Given air correlation parameters are empirically fitted specifically for jet impingement experiments utilizing air data, this difference was expected [27], but the extent was unknown. The percent Nusselt number increase from air to $CO_2$ between a Reynolds number $10^6$-$10^7$ is shown in Table 5.4.

An additional concern is whether or not $CO_2$ will behave as a real gas at primary conditions. The compressibility factor or z-factor is 1.01 for $CO_2$ at primary conditions and thus will act as an ideal gas. For comparison, the z-factor for air at primary conditions is 1.09. Table 5.5 shows the property differences for air and $CO_2$ at primary conditions at a Reynolds number of 249,984. Observing that the thermal conductivity of the fluids is relatively the same, heat will transfer at a similar rate through both fluids. But $CO_2$ has a higher specific heat and density, resulting in a greater capacity to store heat, and thus more heat will transfer from the heated surface to the $CO_2$ resulting in the greater heat transfer as shown in Table 5.4. The exact reason why $CO_2$ provides greater heat transfer is still unknown.

Table 5.4: Increase in Nusselt number from air to $CO_2$

| **$Nu_{CO2}$** | **$Nu_{Air}$** | **Reynolds number** | **Nu % increase** |
|---|---|---|---|
| 182 | 160 | 100,000 | 13% |
| 352 | 300 | 200,000 | 17% |
| 692 | 580 | 400,000 | 19% |
| 1,032 | 860 | 600,000 | 20% |
| 1,372 | 1,140 | 800,000 | 20% |
| 1,712 | 1,420 | 1,000,000 | 21% |

Table 5.5: Property difference in air and $CO_2$ at primary conditions

| | **$CO_2$** | **Air** | **% Difference** |
|---|---|---|---|
| Density ($kg/m^3$) | 159 | 97 | 63% |
| Thermal Conductivity (W/m/K) | 5.47E-02 | 5.48E-02 | -0.24% |
| Kinematic viscosity ($m^2/s$) | 2.12E-07 | 3.64E-07 | -42% |
| Dynamic viscosity (Pa-s) | 3.4E-05 | 3.6E-05 | -5% |
| Pr | 0.76 | 0.72 | 5% |
| Specific heat at constant pressure (kJ/kg/K) | 1229 | 1112 | 11% |

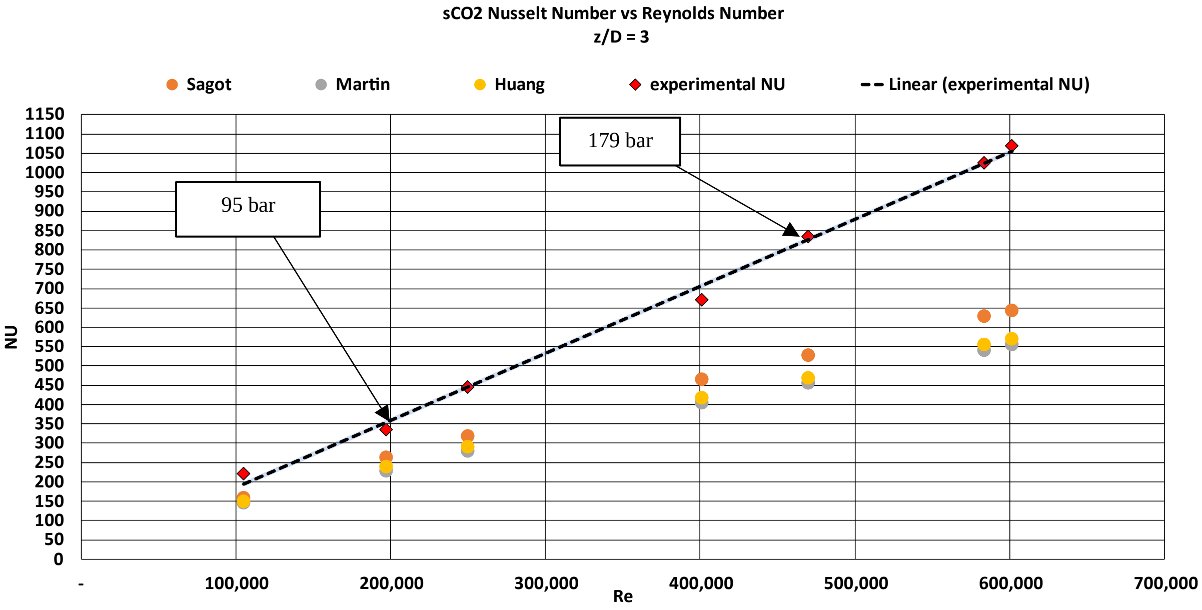

Figure 5.8: $sCO_2$ Rig Test Results z/D= 3 at primary conditions

Figure 5.9 shows the four other tests—the first four tests in Table 5.3— that were performed but did not meet the primary condition of a 400c jet temperature. The trend line for the 400c jet temperature test is shown in Figure 5.8, and the trend line for all the tests is shown in Figure 5.9. The average deviation of the trendline in Figure 5.9 from Figure 5.8 is 11%, and the maximum deviation is 32% at a Reynolds number of $10^6$. Between a Reynolds number of $2 \cdot 10^6$ – $10^{7,}$ the deviation ranged from 8% and 12%.Table 5.3 shows relevant test conditions for all the conducted tests.

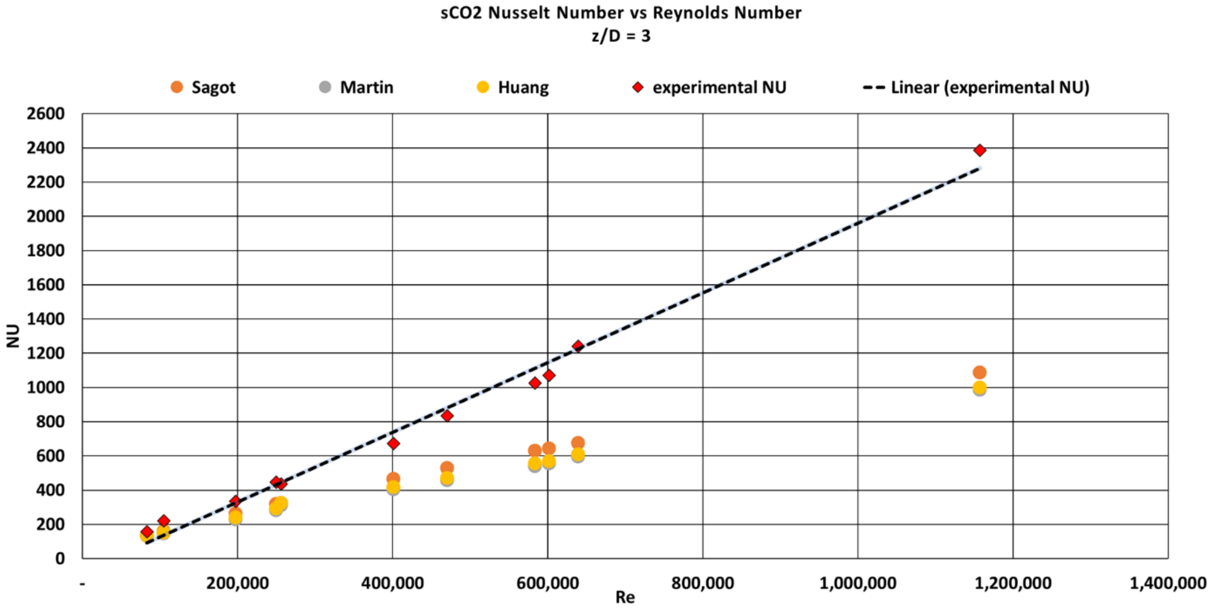

Figure 5.9: Complete $sCO_2$ experimental data set

Given air correlations cannot be used to quantify $sCO_2$ heat transfer, a correlation that can do so is necessary. Using the test at target conditions and manipulating the Martin correlation, a new correlation can be derived, fitting the data. The adjusted Martin correlation is provided below:

$$Nu_{avg} = Pr^{0.42}\frac{D}{r}\frac{1-1.1D/r}{1+0.1\left(\frac{H}{D}-6\right)D/r}0.151Re^{n} \tag{5.1}$$

$for\ 100{,}000 < Re < 360{,}000$, n = 0.8158

$for\ 360{,}000 < Re < 601{,}000$, n = 0.8253

When $T_j \approx 400c$ , $95 < \mathrm{P(bar)} < 210, \frac{\mathrm{H}}{\mathrm{D}} \approx 2.8$.

The parameter n is determined by setting all other variables at the test condition values conducted in this study. Nusselt number is a range of values; thus, a range of n-values will be provided. Averaging the n-values for the Reynolds numbers between 105,000 and 401,000 provided the n-value for fitting the adjusted Martin for Reynolds numbers between 100,000 and 360,000. And averaging the n-values for the Reynolds numbers ranging between 470,000 and 601,000 provided the n-value for fitting the adjusted Martin for Reynolds numbers between 360,000 and 601,000. The deviation of the $sCO_2$ data set at the specified Reynolds numbers from the adjusted Martin correlation is shown in Table 5.6. Figure 5.10 displays the adjusted Martin correlation and the trendline for the $sCO_2$ target conditions data set.

Table 5.6: Adjusted Martin correlation deviation from $sCO_2$ Target Data set

| **Reynolds Number** | **Deviation from $sCO_2$** |
|---|---|
| 105,092.21 | 3% |
| 197,393.27 | 12% |
| 249,984.70 | 3% |
| 401,103.93 | 7% |
| 470,112.60 | 1% |
| 583,443.78 | 6% |
| 601,530.51 | 9% |

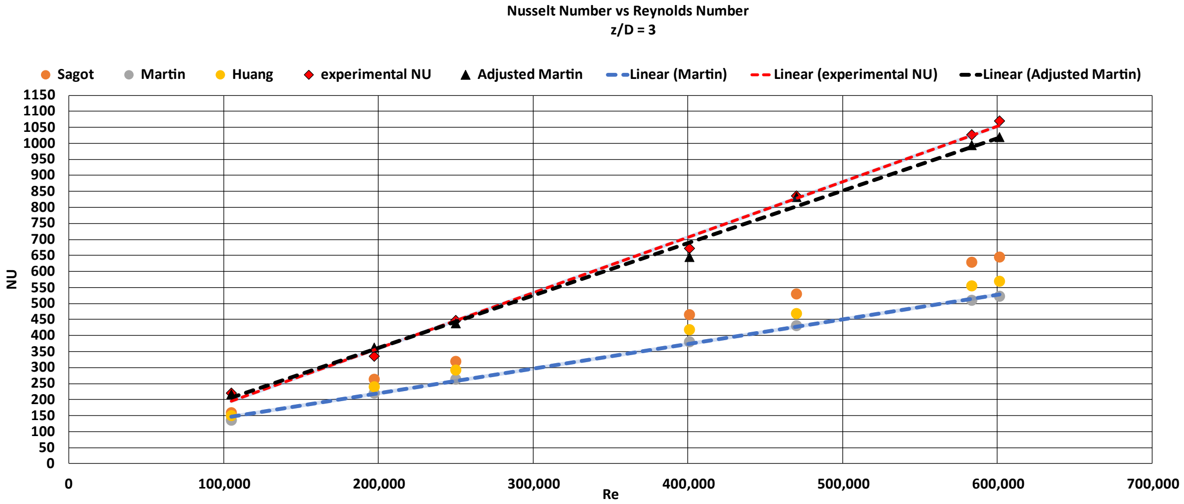

Figure 5.10: Adjusted Martin correlation with $sCO_2$ target data and air correlations

Figure 5.11 shows the same data as Figure 5.9 but with the uncertainty bands at a 95% confidence interval. As discussed earlier in the 'Uncertainty Analysis' section, the uncertainty of the thermocouples is 2.2c. The absurd uncertainty values for Reynolds numbers greater than 256,000 is due to the temperature delta between the jet and the surface being too small to establish a more accurate certainty for the Nusselt number. Table 5.7 shows the temperature delta per test and the total percent contribution to the total error. As the temperature delta increases, the total contribution of its error is minimized. Unfortunately, the maximum supply voltage at test conditions is approximately 17 volts. Even with this limiting factor, a number of the test were performed slightly pasted this value, as shown in Table 5.8, although this did not greatly improve the temperature difference.

Table 5.7: Change in dT error contribution with increasing dT

| **P, T** | **Reynolds number** | **dT** | **% dT is of Total Error** |
|---|---|---|---|
| 197 bar 225c | 1,157,380 | 2.60 | 97.7% |
| 203 bar 320c | 638,993 | 3.16 | 98.0% |
| 202 bar 400c | 601,530 | 4.01 | 96.5% |
| 191 bar 405c | 583,443 | 4.15 | 96.3% |
| 179 bar 413c | 470,112 | 4.85 | 95.3% |
| 197 bar 415c | 401,103 | 5.16 | 95.2% |
| 209 bar 416c | 249,984 | 7.69 | 90.0% |
| 194 bar 413c | 105,092 | 8.53 | 93.6% |
| 95 bar 412c | 197,393 | 10.63 | 82.0% |
| 203 bar 204c | 256,147 | 15.04 | 53.0% |
| 117 bar 154c | 82,932 | 53.47 | 7.0% |

Table 5.8: Test conducted around maximum voltage

| **Tests at Target Conditions** | | | | | | | |
|---|---|---|---|---|---|---|---|
| Reynold Number | 601,531 | 583,444 | 470,113 | 401,104 | 249,985 | 105,092 | 197,393 |
| dT | 4.01 | 4.15 | 4.85 | 5.16 | 7.69 | 8.53 | 10.63 |
| Voltage | 18.94 | 19.04 | 18.56 | 17.05 | 16.97 | 12.56 | 16.73 |

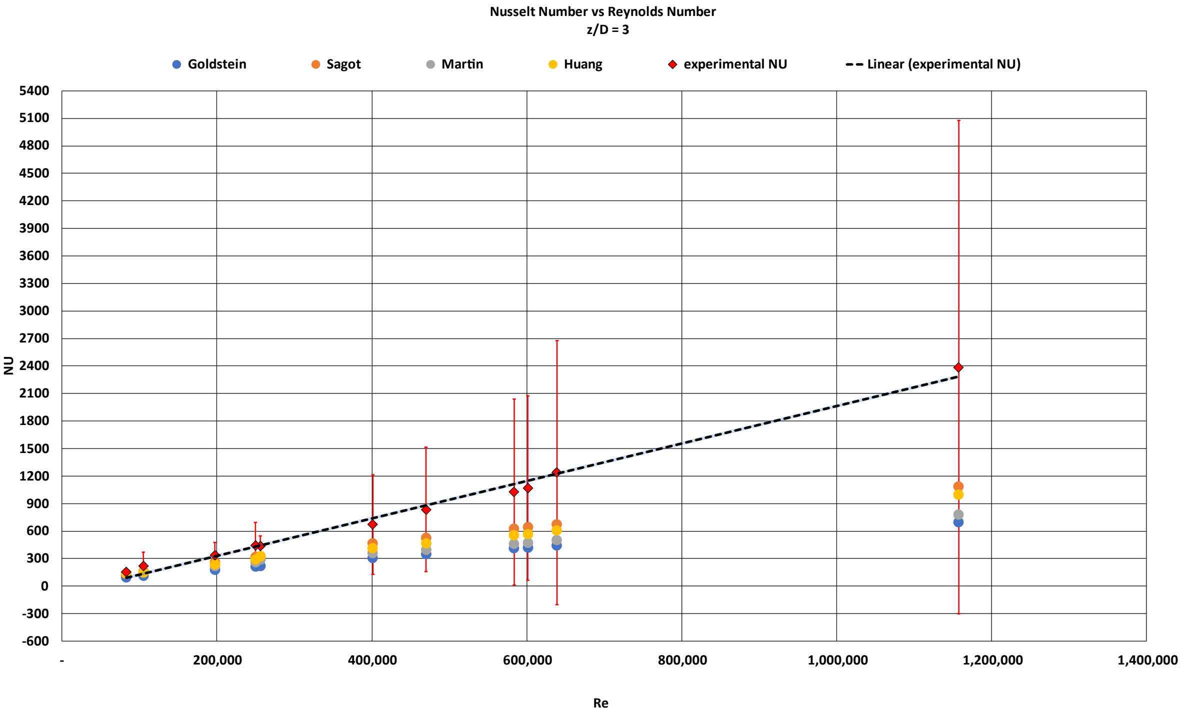

Figure 5.11: $sCO_2$ data with 95% Confidence Interval

# CHAPTER 6: CONCLUSION

The experiments performed in this study investigate the heat transfer capability of supercritical $CO_2$ ($sCO_2$) for single-jet impingement. The heat transfer data collected is the first available for $sCO_2$ impingement studies and design. A Benchtop test is first performed to validate the heat transfer methodology, data reduction, and data acquisition systems. Then, the second set of tests are performed within the test Rig to validate the experimental apparatus and the procedures of concern in the benchtop test. The experimental air Nusselt numbers for the benchtop and Rig tests show good agreement with the correlation and CFD. The primary conditions for the $sCO_2$ experiments were to maintain a jet temperature of 400c at a pressure of 200 bar. Although for a number of tests, these conditions varied due to an assortment of factors. Reynolds number was varied between 80,000 and 1,000,000 to quantify how the heat transfer would change with increasing flow rate. As expected, the Nusselt number linearly increased with the Reynolds number.

The collected results show that $sCO_2$ jet impingement provides substantially more heat transfer than predicted by air-derived correlations. Experimental air data is used to derive the air correlations; thus, capturing the heat transfer capability of $CO_2$ would be outside of their abilities. Therefore, a $sCO_2$ correlation is derived using the experimental data from the test condition of this study to provide a more accurate prediction of the heat transfer. The $sCO_2$ correlation is obtained by modifying the Martin correlation. The modified correlation is limited to the primary conditions of this study shown in equation 5.1.

# CHAPTER 7: FUTURE WORKS

The $sCO_2$ impingement heat transfer results provided here will be the only data set available for use at the time of the completion of this investigation. Future works will validate the $sCO_2$ data collected and expand the Reynolds number range. In addition, tests with significantly less uncertainty are a necessity. Experiments with varied jet temperatures with constant Reynolds number or mass flow with CFD experiments can provide additional insights into the cooling capabilities of $sCO_2$. A particle image velocimetry (PIV) study would also supply useful knowledge on the structure of the flow.

# REFERENCES

[1] Liu, Z., 2015, “Supply and Demand of Global Energy and Electricity,” Global Energy Interconnection, pp. 101–182.

[2] Cengel, Y. A., and Boles, M. A., 2005, *Thermodynamics: An Engineering Approach*, McGraw-Hill Education, London, England.

[3] Kaewchoothong, N., Maliwan, K., Takeishi, K., and Nuntadusit, C., 2017, “Effect of Inclined Ribs on Heat Transfer Coefficient in Stationary Square Channel,” Theor. Appl. Mech. Lett., **7**(6), pp. 344–350

[4] Nelson, E. S., and Reddy, eds., 2020, *Green Aviation: Reduction of Environmental Impact through Aircraft Technology and Alternative Fuels: Reduction of Environmental Impact through Aircraft Technology and Alternative Fuels*, CRC Press, London, England.

[5] Amano, R. S., ed., 2014, *Impingement Jet Cooling in Gas Turbines*, WIT Press.

[6] Jabbarli, A., 2018, “Effect of Chamfered Nozzle Geometry on Impinging Jet Flow.”

[7] Yang, J., Lian, H., Liang, W., Nguyen, V. P., and Chen, Y., 1997, “Experimental Investigation of the Effects of Supercritical Carbon Dioxide on Fracture Toughness of Bituminous Coals,” Int. J. Rock Mech. Min. Sci, **107**, pp. 233–242.

[8] Khadse, A., 2020, *Supercritical CO2 Heat Transfer Study Near Critical Point in a Heated Circular Pipe*.

[9] James W. Gauntner, John N.B. Livingood, and Peter Hrycak, 1970, *Survey of Literature on Flow Characteristics of a Single Turbulent Jet Impinging on a Flat Plate*.

[10] Viskanta, R., 1993, “Heat Transfer to Impinging Isothermal Gas and Flame Jets, ” Exp,” Exp. Therm. Fluid Sci, **6**(2), pp. 111–134.

[11] Zuckerman, N., and Lior, N., 2006, “Jet Impingement Heat Transfer: Physics, Correlations, and Numerical Modeling,” *Advances in Heat Transfer*, Elsevier, pp. 565–631.

[12] Bradbury, L. J. S., 1965, “The Structure of a Self-Preserving Turbulent Plane Jet,” J. Fluid Mech., **23**(01), p. 31.

[13] Martin, H., 1977, “Heat and Mass Transfer between Impinging Gas Jets and Solid Surfaces,” *Advances in Heat Transfer*, Elsevier, pp. 1–60.

[14] Maurel, S., and Solliec, C., 2001, “A Turbulent Plane Jet Impinging Nearby and Far from Aflat Plate,” Exp, **31**, pp. 687–696.

[15] Han, B., and Goldstein, R. J., 2001, "Jet-Impingement Heat Transfer in Gas Turbine Systems," Ann. N. Y. Acad. Sci., **934**(1), pp. 147–161.

[16] Kataoka, K., Sahara, R., Ase, H., and Harada, T., 1987, "Role of Large-Scale Coherent Structures in Impinging Jet Heat Transfer," J. Chem. Eng. Japan, **20**(1), pp. 71–76.

[17] Hrycak, P., 1981, *Heat Transfer From Impinging Jets A Literature Review*, Air Force Wright Aeronautical Laboratories, Wright-Patterson AFB OH.

[18] Huang, G. C., 1963, "Investigations of Heat-Transfer Coefficients for Air Flow through Round Jets Impinging Normal to a Heat-Transfer Surface," J. Heat Transfer, **85**(3), pp. 237–243.

[19] Brdlik, P. M., and Savin, V. K., 1965, "Heat Transfer between an Axisymmetric Jet and a Plate Normal to the Flow," Journal of Engineering Physics, **8**(2), pp. 91–98.

[20] Lytle, D., and Webb, B. W., 1994, "Air Jet Impingement Heat Transfer at Low Nozzle-Plate Spacings," Int. J. Heat Mass Transf., **37**(12), pp. 1687–1697.

[21] Chen, K., Xu, R.-N., and Jiang, P.-X., 2018, "Experimental Study of Jet Impingement Cooling with Carbon Dioxide at Supercritical Pressures on Micro Structured Surfaces," J. Supercrit. Fluids, **139**, pp. 45–52.

[22] Chen, K., Xu, R.-N., and Jiang, P.-X., 2018, "Numerical Investigation of Jet Impingement Cooling of a Low Thermal Conductivity Plate by Supercritical Pressure Carbon Dioxide," Int. J. Heat Mass Transf., **124**, pp. 1003–1010.

[23] Kim, S. H., Lee, N., Lee, H., Bang, M., and Cho, H. H., 2017, *A Numerical Study of Heat Transfer Characteristics of S-CO2 Impinging Jet for Direct Fired Oxy-Fuel s-CO2 Turbine*.

[24] Cormier, I. J., Curbelo, A., Khadse, A., and Kapat, J., 2021, "A RANS Approach to Supercritical CO2Single-Jet Impingement at Ultra-High Reynolds Numbers," *AIAA Scitech 2021 Forum*, American Institute of Aeronautics and Astronautics, Reston, Virginia.

[25] Adeoye, S., Parahovnik, A., and Peles, Y., 2021, "A Micro Impinging Jet with Supercritical Carbon Dioxide," Int. J. Heat Mass Transf., **170**(121028), p. 121028.

[26] 2019, "SwRI and GE Design and Operate the Highest Temperature SCO2 Turbine in the World," Southwest Research Institute [Online]. Available: https://www.swri.org/press-release/swri-ge-highest-temperature-sco2-turbine-world. [Accessed: 27-Oct-2022].

[27] Martin, H., 1977, "Heat and Mass Transfer between Impinging Gas Jets and Solid Surfaces," *Advances in Heat Transfer*, Elsevier, pp. 1–60.

[28] Huang, L., and El-Genk, M. S., 1994, "Heat Transfer of an Impinging Jet on a Flat Surface," Int. J. Heat Mass Transf., **37**(13), pp. 1915–1923.

[29] Sagot, B., Antonini, G., Christgen, A., and Buron, F., 2008, "Jet Impingement Heat Transfer on a Flat Plate at a Constant Wall Temperature," Int. J. Therm. Sci., **47**(12), pp. 1610–1619.

[30] Goldstein, R. J., Behbahani, A. I., and Heppelmann, K. K., 1986, "Streamwise Distribution of the Recovery Factor and the Local Heat Transfer Coefficient to an Impinging Circular Air Jet," Int. J. Heat Mass Transf., **29**(8), pp. 1227–1235.

[31] Test Uncertainty, A., 2005, "Ptc 19.1-2005"," American Society of Mechanical Engineers, 3, pp. 10016–15990.

[32] Harvey, A. H., Bell, I. H., Huber, M. L., Laesecke, A. R., Lemmon, E. W., Meyer, C. W., Muzny, C. D., and Perkins, R. A., 2016, Thermophysical Properties of Carbon Dioxide and Co2-Rich Mixtures.